HYDROGEN INTERACTION WITH AL(111) AND TI-DOPED AL(111) SURFACES FOR H STORAGE APPLICATIONS

BY STEFAN P. SCHAEFER

A thesis submitted to the

Graduate School—New Brunswick

Rutgers, The State University of New Jersey

in partial fulfillment of the requirements

for the degree of

Master of Science

Graduate Program in Physics and Astronomy

Written under the direction of

Prof. Yves J. Chabal

and approved by

_____

_____

_____

New Brunswick, New Jersey

October, 2007

ABSTRACT OF THE THESIS

Hydrogen Interaction with Al(111) and Ti-doped Al(111) Surfaces for H Storage Applications

by Stefan P. Schaefer

Thesis Director: Prof. Yves J. Chabal

Complex metal hydrides are promising candidates for hydrogen storage applications. Most of these materials consist of aluminum mixed with other elements. It was found that titanium doping allows their use in a convenient temperature and pressure range. Therefore the key process is the dissociation of molecular hydrogen at a Ti catalyst on the surface. Preliminary studies with pure and titanium-doped aluminum surfaces are undertaken to gain a basic understanding of the hydrogen adsorption mechanism.

The interaction of hydrogen with an Al(111) surface was studied using Infrared Reflection Absorption Spectroscopy (IRRAS) under Ultra High Vacuum (UHV) conditions. Hereby the formation of aluminum hydrides (alanes) in different sizes was observed depending on the hydrogen coverage of the surface. The growth of larger alanes is favored at higher H exposures. Different measurements were carried out for temperatures of 93, 180 and 259K and it was found that larger alanes form at higher temperatures.

In another step of the experiment an Al surface was doped with titanium atoms emitted from a home-built Ti-source. Ti structures with a thickness of less than one monolayer (ML) were grown at 105K and a Ti film of around one ML was deposited at room temperature. The deposition rate was determined with a quartz crystal monitor and the deposition on the surface could be verified by Auger Electron Spectroscopy

(AES). Low Energy Electron Diffraction (LEED) patterns were recorded before and after different Ti-depositions and were always showing the typical hexagonal symmetry for the closed packed (111) surface of the fcc Al crystal.

To compare the vibrational modes of alanes forming on Al(111) surfaces with the ones of solid state AlH_3 Fourier Transform Infrared Spectroscopy (FTIR) was performed in a different setup using a high vacuum. No matches of the frequencies could be found but the decomposition of AlH_3 to Al and H could be observed at temperatures higher than 170°C.

Acknowledgements

I would like to thank Dr. Jean-Francois Veyan for his help and support. He taught me how to handle a UHV system and without him this work would have been a lot harder. Moreover I want to thank Daniel Mayer and John Landers for helpful discussions. My special thanks go to Prof. Yves J. Chabal for advising me.

Dedication

Dedicated to my parents.

Table of Contents

Abstract ii

Acknowledgements iv

Dedication v

List of Figures ix

1. Motivation 1

2. Experimental Setup 5

2.1. The UHV-chamber 5

2.2. Auger Electron Spectroscopy (AES) 8

2.3. Low Energy Electron Diffraction (LEED) 9

2.4. Quadrupole Mass Spectrometer 11

2.5. Bayard-Alpert-Gauge 14

2.6. Sputter Ion Gun 14

2.7. Turbomolecular Pumps 14

2.8. Ion Pumps 16

2.9. The Ti-Source 16

3. Fourier Transform Infrared Spectroscopy 18

3.1. Infrared Spectroscopy and Molecular Vibrations 18

3.2. Basics of Fourier Transform Infrared Spectroscopy (FTIR) 20

3.3. Infrared Reflection Absorption Spectroscopy (IRRAS) 25

3.4. Fourier Transform Infrared Spectroscopy in our Experiment 26

4. Sample Preparation 28

4.1. Cleaning the Sample 28
4.2. Checking the Cleanliness of the Sample 29

5. Hydrogen on Al(111) 32
5.1. Introduction 32
5.2. Experimental Procedure 33
5.3. Results and Discussion 34
5.3.1. Low Hydrogen Exposures at 93K 34
5.3.2. Different Hydrogen Exposures at 93K 36
5.3.3. Hydrogen Exposures at 250K 39
5.3.4. Hydrogen Exposure at 180K 41
5.3.5. Saturation for Hydrogen Adsorption at Different Temperatures . 43
5.3.6. Effects of Surface Roughness on Alane Formation. 44
5.4. Conclusion 45

6. Titanium Doping of the Al(111) Surface 47
6.1. Introduction 47
6.2. Experimental Procedure 49
6.3. Results and Discussion 50
6.3.1. Low Ti-Depositions at T=105K 50
6.3.2. Low Ti-Depositions at Room Temperature 52
6.3.3. Higher Ti-Depositions at Room Temperature 53
6.4. Conclusion 60

7. Infrared Study of Solid State Aluminum-Hydride 62
7.1. Introduction 62
7.2. Experimental Procedure 63
7.3. Results and Discussion 64
7.3.1. Alanes Mixed with KBr 64
7.3.2. Evolution with Temperature 66

7.3.3. Pure Alanes 67
7.3.4. Comparison Between Pure Alanes and Alanes Mixed with KBr . 68
7.3.5. Comparison Between Solid State Alanes and Alanes on Al(111) . 70
7.4. Conclusion 70

8. Summary 72

References 74

List of Figures

1.1. Volume of 4 kg hydrogen in different storage approaches compared to the size of a car (taken from [1]). 3

2.1. Schematic top view of the UHV chamber that was used for the experiment. 5

2.2. Schematic drawing of the two pumping chains which are used on the UHV chamber. Each pumping system is represented by one color. 7

2.3. Schematic view of the process which takes place during Auger Electron Spectroscopy (AES) (taken from [2]) 8

2.4. Schematic setup for Low Energy Electron Diffraction (taken from [2]) . . 11

2.5. Quadrupole mass spectrometer. Ions are produced in ionizer and only the ones with a specific charge-to-mass ration can pass the quadrupole rods and be detected by a Faraday-cup. (taken from [3]) 12

2.6. Mass spectrum recorded under UHV conditions. The peaks N, CH_3 O_2 and C_2H_6 and the height of the CO or N_2 peak are indications, that there was a leak in the UHV chamber when this spectrum was taken. 13

2.7. Cut trough of a Turbomolecular pump (taken from [4]). 15

2.8. The top part of the self-build Ti-source. A hot tungsten filament emits electrons which are accelerated towards a titanium piece where they heat it up until it sublimes and its atoms evaporate from the surface. 16

3.1. Picture of the used Fourier Transform Spectrometer with artificially added IR-beamline. 21

3.2. Schematic drawing of the optics which were used for the IR- and the laser-beam (not to scale). 22

3.3. A typical interferogram, i.e. intensity distribution over the optical path difference, with the ZPD in the middle. 23

3.4. The corresponding spectrum to the interferogram shown in figure 3.3. . . 24
3.5. An incoming electromagnetic wave can be divided into a perpendicular and parallel component which leads to different polarization effects on the surface of a metal (modified from [5]). 25
4.1. Typical AES of Al(111) before the cleaning processes. The main contaminations O, C and Ti are clearly visible in this spectrum while the intensity of the Ar peak is very week. 29
4.2. Auger spectra before, after sputtering and after annealing. An amplification of 20 was used to record these spectra. 30
4.3. Leedpattern of a clean Al(111) surface recorded at an energy of 53.5 eV. The hexagonal symmetry certifies that the probed sample shows a closed packed surface as expected for Al(111). 31
5.1. STM picture of alanes (white spots) on a now etched Al(111) surface. The total width of the surface part shown in the picture is 5000 Å (taken from [6]). 33
5.2. Two low hydrogen exposures at 93K. The peak C around 1790 cm^{-1} corresponds to adsorbed H on step-edges while the peaks at 1875 and 1860 cm^{-1} are terminal stretching bands of H bond to alanes (A) and Al (B). 34
5.3. A hydrogen exposure of 60L at 93K. The main peak A at 1875 cm^{-1} results form alanes on terraces. Furthermore there are some new structures growing at 1550 to 1600 cm^{-1} (E) and 1640 to 1760 cm^{-1} (D). 36
5.4. Different hydrogen exposures at 93K. For higher H doses there are indications for the formation of bigger alanes. 37
5.5. Integrated area from 2000 to 1400 cm^{-1} of the spectra after different H exposures. The hydrogenation can be described by a three step model. . 38
5.6. Comparison of spectra of a 60L hydrogen exposure at 90 and 250K. . . . 39
5.7. Spectra of different hydrogen exposures at 250K. 40
5.8. Spectra of different hydrogen exposures at 180K. 42

5.9. Spectra of a saturated Al surface after H-adsorption at 93K (540L), 180K (480L) and 250K (420L). 43
5.10. Hydrogen exposures and re-exposures after H desorption for low and saturation coverage. Apparently the alane formation is reduced by increasing surface roughness. 44
5.11. Schematically picture for H adsorbed to the etched surface. The signal of the atoms in the gaps is screened due to the high absolute value of n. 45
6.1. Different models describing the growth of an overlayer on a substrate together with its characteristic variation of the Auger peak intensity (taken from [2]) 48
6.2. Set of AES spectra during Ti deposition at T=105K. The inset shows the evolution of the Al peak. To make the height differences more clearly the later peaks are shifted to the right. 51
6.3. LEED patterns at an energy of 214.5 eV for low depositions at T=105K 52
6.4. Evolution of the Al peak 68 eV and the Ti-peaks at 387 and 418 eV for low exposures at T=290K. Apparently the height of the carbon (272 eV) and oxygen (503 eV) contamination stays almost the same. 53
6.5. LEED patterns at an energy of 93.0 eV for low depositions at T=290K . 54
6.6. Set of AES spectra during Ti deposition at T=300K. The inset shows the evolution of the Al peak. To make the height differences more clearly the later peaks are shifted to the right. 55
6.7. Evolution of the low energy Ti peak in comparison with the Al peak. . . 56
6.8. LEED patterns which were observed in our experiment at an energy of 53.5 eV in comparison with LEED pictures from the literature [7] recorded at 52.8 eV. 59
6.9. Set of AES spectra showing the decreasing of the Ti double peak due to sputter-cleaning of the surface. Apparently most of the Ti overlayer could be already removed with 6 sputtering cycles. 60

7.1. Different AlH_3 samples: Mixture of AlH_3 and KBr after (a) and before (b) annealing to 250°C; Pellets out of pure AlH_3 after (c) and before (d) annealing to 250°C 63
7.2. The cell in the Thermo Nicolet Nexus 670 spectrometer which was used for investigating the solid state AlH_3. 64
7.3. Spectrum of a solid state AlH_3 sample recorded in a pumped and baked cell. 65
7.4. Difference of the absorbance after the solid state AlH_3 sample was annealed to 350°C. 66
7.5. Absorbance of the solid state AlH_3/KBr sample as function of temperature (from 115°C to 250°C). 67
7.6. Absorbance of a pure solid state AlH_3 sample after annealing to 250°C. 68
7.7. Absorbance between the not annealed and the annealed sample for pure solid state AlH_3 and alanes mixed with different amounts of KBr. 69
7.8. Comparison of the vibrational bands between solid state Alanes and Alanes on Al(111). 70

Chapter 1

Motivation

Finding a proper material for hydrogen storage is one of the key steps on the way to a future hydrogen economy. Currently most vehicles are powered by combustion engines using hydrocarbons as fuel. Replacing this conventional fuel by hydrogen would result in several advantages:

Hydrogen is attractive for use as a fuel because with 142 MJ kg^{-1} its chemical energy per mass is very high. This can be explained by the fact, that there is only one proton for every valence electron which can form bondings and thereby free energy. To reach the same amount of energy nearly three times the mass of gasoline is required [1]. Using hydrogen makes it possible to operate fuel-cells where hydrogen reacts with oxygen and forms water in an exothermic reaction. This process could reach an energy efficiency of 60%, which is more than twice as much as in combustion engines because they are not limited by the Carnot efficiency [1]. But even if a lean hydrogen oxygen mix is burned in a conventional combustion engine the only exhausted gas is water vapor [1] which makes it a very environmentally friendly fuel and could significantly reduce the CO_2 output. Moreover both the educts (hydrogen, oxygen) and the product (water) of the reaction are non toxic elements which prevents the environment or people from being poisoned in case of a leak or accident. Hydrogen is the most common element on Earth even though only 1% can be found in form of a molecular gas and most of the H-atoms are bound in water molecules or in hydrocarbons [1]. Another important issue is that using hydrogen instead of gasoline could, depending on how the H_2 is produced, reduce the dependence on petroleum imports. Currently around two-thirds of the 20 million barrels of oil consumed in the United States per day are needed for the transportation sector. 55% of this oil must be imported and this trend is increasing in the next years.

Possibilities for the production of hydrogen using domestic resources such as renewable (for example solar) or nuclear energy are also being investigated at the moment [8].

Unfortunately there are also some problems that have to be solved first. The most striking one is that under atmospheric pressure and room temperature gaseous hydrogen occupies a very high volume. For example 4 kg of gaseous H_2 has a volume of 45 m^3 [1] which makes it impossible to transport it on-board a car. Furthermore H_2 can diffuse through most of the common tank materials including stainless steel because of its small size. Some security concerns arise since hydrogen contains a lot of free energy which can also be burned in an uncontrolled way. The typical chemical high school experiment where small balloons of H_2 explode when they come in contact with a glowing wood piece or famous historical accidents like the Hindenburg catastrophe are only some examples for this problem. Finally there is also the economic point of view. Today hydrogen is still relatively expensive when compared to gasoline which will hopefully be changed by new or improved mass production methods. Most of these problems must be overcome by the desired on-board energy storage which should be light and compact but also safe and affordable [1].

The U.S. Department of Energy started the National Hydrogen Storage Project as part of the Hydrogen Fuel Initiative in 2003 to focus all the research and development efforts in this area. The aim of this program is to find a storage medium that allows designing further vehicles which have the same performance as today's hydrocarbon powered cars at a similar price. This includes a driving range of at least 300 miles (around 500km) per tank filling and short refuel times. Currently the most significant targets are to provide a storage system which contains at least 6% gravimetric hydrogen density (which results in 2kWh/kg) and a volumetric energy density of 1.5 kWh/l. Moreover it has to be able to release H in pressure and temperature regions which are normal for operating fuel cells and the life cycle of the system should exceed 1000 refulling times [8].

In general there are two different approaches for hydrogen storage for automobile applications. The tank can either be on-board the vehicle and be refueled at a fuel

station or the whole storage system has to be replaced every time and be recharged off-board. Here only the on-board storage technologies are discussed. There are mainly four technological attempts to realize a mobile H storage system: Hydrogen can either be held under high pressure, liquefied, adsorbed on solids of large surface area or stored in a solid for example in metal hydrides [9]. Figure 1.1 shows the volume of 4 kg hydrogen in contrast to the size of a car for different storage possibilities.

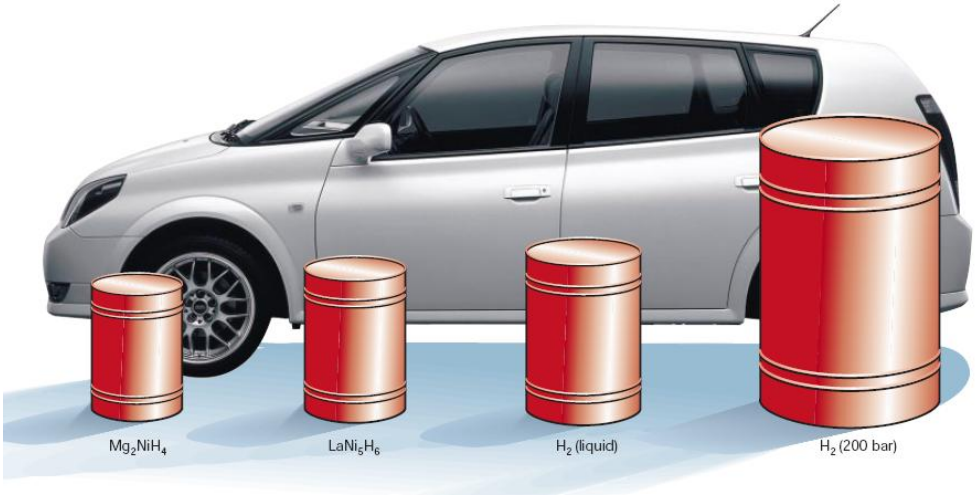

Figure 1.1: Volume of 4 kg hydrogen in different storage approaches compared to the size of a car (taken from [1]).

Tanks for hydrogen storage out of carbon fiber-reinforced materials for pressures up to 700 bar (10000 psi) have been developed and are currently being tested [8]. The problem is that 4 kg of hydrogen at a pressure of 200 bar, which would allow a fuel cell operated car to drive 400 km, still needs a volume of 225 liters [1]. Storage systems for higher pressures are expensive and there are also some security concerns about using them in daily life on normal streets [9].

With 70.8 kg m^{-3} liquid hydrogen offers a good volumetric density. But unfortunately it has a condensation temperature of -252°C at 1 bar [1] which leads to a loss of over 30% of its heating value only for liquefying the H_2. Furthermore because of insufficient thermal isolation there is still a boil-off-rate of approximately 1% a day [9]. This results in a higher refueling frequency, higher costs, worse energy efficiency and safety problems especially if the car is parked in a closed building such as a garage [8].

The third possibility is to physisorb molecular hydrogen on solids with high surface areas. Several materials like single-walled carbon nanotubes, graphine materials and metallic organic frameworks are under investigation. But up to now material could be found which provides a reversible hydrogen storage density to meet the DOE's requirements [8].

Also some metal hydrides show promising features for hydrogen storage. That's why some complex light hydride systems like sodium alanate ($NaAlH_4$ and Na_3AlH_6) are being investigated closely. Bogdanovic and Schwickardi discovered that this material can release hydrogen in the right pressure and temperature range when it is doped with titanium [10]. The reversible hydrogenation of $NaAlH_4$ takes place in two steps and can be described by the following reactions [11]:

$$3NaAlH_4 \rightleftharpoons Na_3AlH_6 + 2Al + 3H_2 \tag{1.1}$$

$$2Na_3AlH_6 \rightleftharpoons 6NaH + 3Al + 3H_2 \tag{1.2}$$

The first reaction can release 3.7 wt% hydrogen and takes place above 33°C while the second one releases 1.8 wt% H_2 at temperatures over 110°C [11]. This gives this material a theoretical gravimetric capacity of 5.5 wt%. In practice only around 4 wt% can be reached which is below the DOE targeted 6 wt% [8]. However this system provides the possibility of studying the roll of a catalyst in a complex metal hydride and to investigate other open questions in the reaction mechanism.

That's why our project at Rutgers University and Brookhaven National Labs was set up. We will focus on surface phenomena to understand the effect of the Ti catalyst on reversible hydrogen storage. Scanning Tunneling Microscopy (STM) and Low Energy Electron Microscopy (LEEM) investigations are in progress at Brookhaven along with Density Functional Theory calculations while here at Rutgers infrared spectroscopy is being conducted. To get a fundamental understanding of the system preliminary studies concerning hydrogen on pure and Ti-doped aluminum surfaces are undertaken. This thesis will show some results of this effort.

Chapter 2

Experimental Setup

2.1 The UHV-chamber

The whole experiment was accomplished under Ultra High Vacuum (UHV) conditions and therefore a UHV chamber out of stainless steel with five view ports and two KBr-IR-windows was used. Figure 2.1 shows a schematic top view of the chamber with some of its instruments.

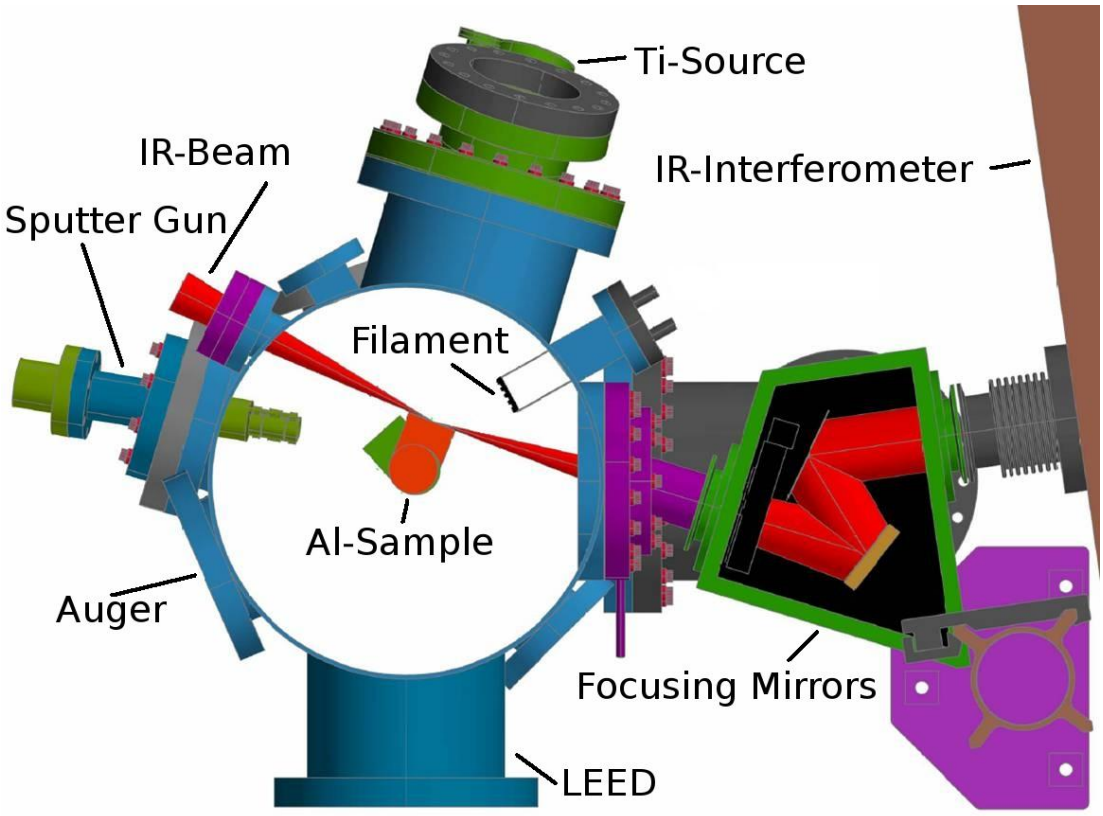

Figure 2.1: Schematic top view of the UHV chamber that was used for the experiment.

In the first part of this work the (111) surface of a single crystal aluminum sample with the surface diameters of 2.5 × 1 cm was investigated. The sample is attached to a manipulator and located in the middle of the chamber. This enables the experimenter to bring it in the desired position by rotating it from 0° to 360° and varying the height. Heating wires in the back of the sample make it possible to anneal the crystal up to 500°C. Moreover the sample can be cooled down to around 90 K by filling the manipulator with liquid nitrogen. The temperature of the crystal can be measured by a thermo-couple and an amperemeter is connected to monitor the current in the sample.

The main analytic instrument is a Fourier-Transform-IR-Spectrometer which makes it possible to conduct Infrared Reflection Absorption Spectroscopy (IRRAS) measurements. Because this is the most important experimental method of this work a more detailed description of this technique can be found in a separate chapter. A system of mirrors focuses the IR beam through a KBr entrance window on the sample with a grazing incidence angle of about 5°. Then the IR beam is reflected by the Al surface and leaves the chamber through the KBr exit window where the beam is focused again and the signal is collected by a detector. KBr windows are used, because they are transparent for mid-IR-radiation but they are still stable enough to withstand the high pressure differences in a UHV-chamber and temperature changes up to 115°C during baking.

Other analytic systems like Auger Electron Spectroscopy (AES), Low Energy Electron Diffraction (LEED) and a water cooled quartz-crystal-monitor are also installed in the chamber. A sputter ion gun is used for cleaning the sample, a Ti-source enables us to deposit titanium on the surface and a tungsten filament can be brought to very high temperatures to dissociate hydrogen molecules.

Figure 2.2 shows a schematic drawing of the two pumping chains which are used to pump our system. The main chamber is pumped down by one turbo molecular pump and two ion pumps. Because the turbopump needs a fore vacuum for its exhaust a rough pump is operated to create it. Another rough pump is used to bring the IR-interferometer to a low vacuum and for differential pumping of the first stage of the manipulator. Differential pumping is a technique where different connected parts of the

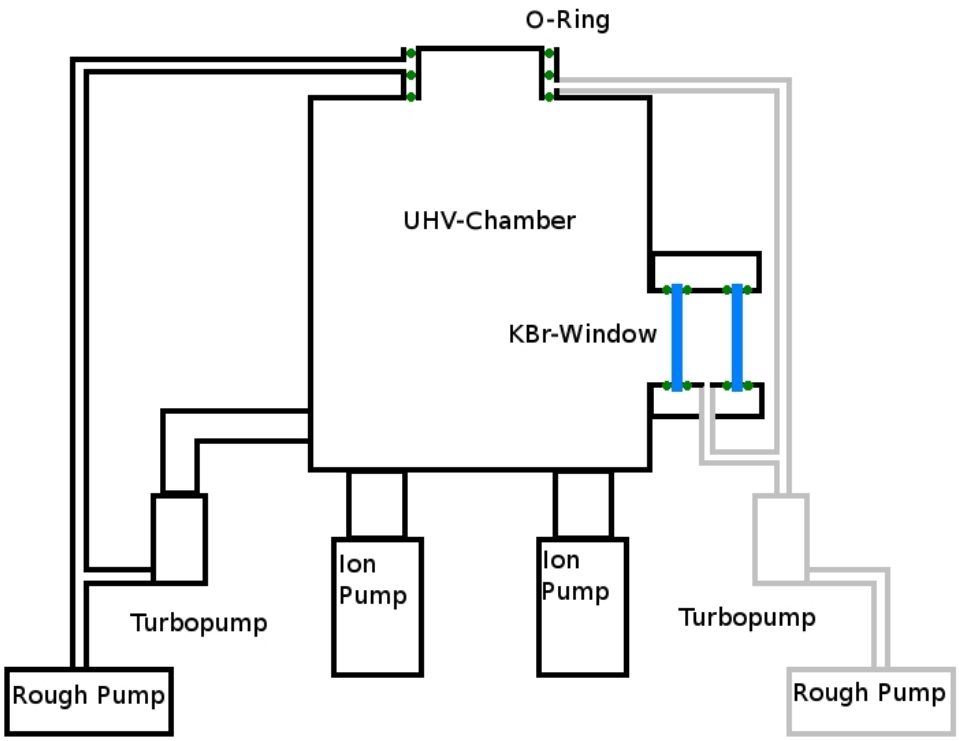

Figure 2.2: Schematic drawing of the two pumping chains which are used on the UHV chamber. Each pumping system is represented by one color.

system are held on different pressures. The area close to room pressure is only pumped to a low vacuum while the next following compartment contains a higher vacuum. The moving parts between two compartments are separated by O-rings. This makes it possible to reach a very low pressure in the main chamber without losing the ability to rotate parts wherefore a rubber sealing is needed. A second turbopump/rough pump combination is used for pumping of the second stage of the manipulator and for differential pumping of the KBr exit window. Moreover the Mercury Cadmium Telluride (MCT) detector is pumped down by this turbopump when it is installed on the chamber. The best pressure which can be reached inside the main chamber is $1.2{\cdot}10^{-10}$ Torr.

Two Bayard-Alpert-Gauges make it possible to measure the pressure in the UHV chamber and in the pumping line. The composition of the residual gas can be checked by a Quadrupole Mass Spectrometer.

In the following sections the most important devices are described and some theoretical background of their functionality is provided.

2.2 Auger Electron Spectroscopy (AES)

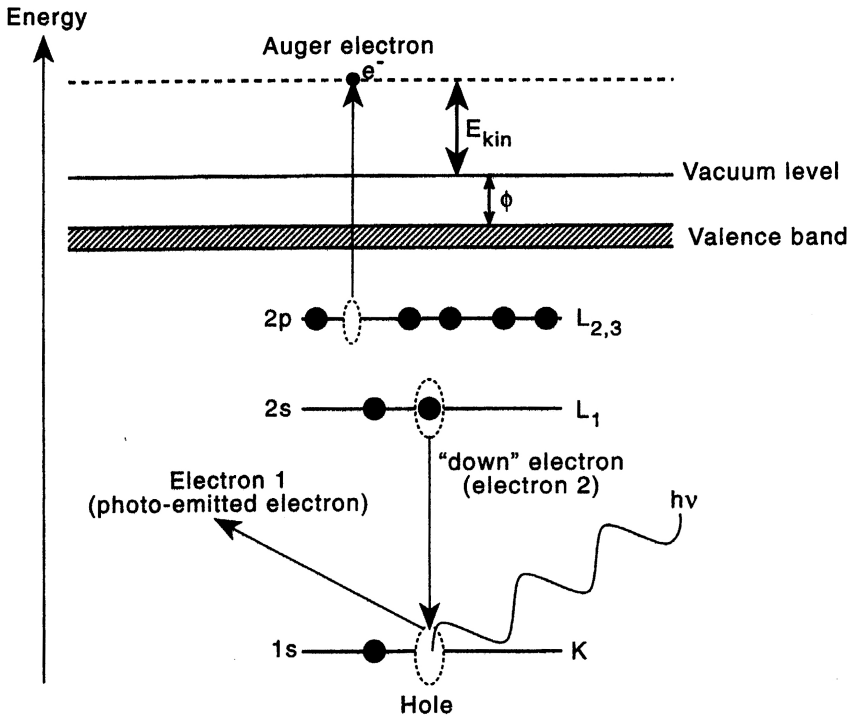

Figure 2.3: Schematic view of the process which takes place during Auger Electron Spectroscopy (AES) (taken from [2])

Auger electron spectroscopy (AES) is a powerful tool to identify the elemental composition of a surface by measuring the energy of an emitted "Auger electron". The whole process is shown in figure 2.3. A surface is being bombarded with photons or in most technical applications with electrons to eject a core level electron. In this way a vacancy, or hole, is created in one of the inner shells. After that a second electron, often called the "down electron", transits to this hole from a higher shell. Thereby the energy difference ΔE between the two shells is freed. This energy is transferred in a third process where either in the case of X-ray fluorescence a photon is emitted from the atom or, in the case of AES, another electron is emitted into vacuum. The kinetic energy of this "Auger electron" can be measured by a detector and is given by the equation

$$E_{kin} = E_{hole} - E_{down} - E_{up} \tag{2.1}$$

where E_{up} is the energy level of the electron which is emitted from an upper shell. All energies in equation 2.1 are energy levels of the corresponding electrons in the atom referenced to the vacuum level. Hence the kinetic energy is independent of the energy of the incident beam and only dependents on the electron's position in the shell of the atom which makes AES element specific [2].

On our chamber a Physical Electronic Industries Model 10-155 Cylindrical Auger Electron Optics apparatus is mounted.

2.3 Low Energy Electron Diffraction (LEED)

In Low Energy Electron Diffraction (LEED) monochromatic electrons are elastically back scattered from the surface of a sample. If the sample has a periodic structure for some electron energies a LEED pattern, which shows the reciprocal lattice of the surface, can be observed.

Constructive interference between scattered electron waves can be found when the path length difference is equal to an integral number of wavelengths λ. In the simplest case of only one dimension and a normal incident beam the equation

$$n\lambda = a \sin \theta_a \tag{2.2}$$

holds, whereby a is the lattice constant in this dimension and θ_a is the angle under which the electrons are scattered. The relation between λ and the magnitude of the incident wavevector $\vec{k}_0$ is given by

$$|\vec{k}_0| = \frac{2\pi}{\lambda}. \tag{2.3}$$

Thus for $\vec{k}_{\|}$, the component parallel to the surface of the incident beam, follows

$$|\vec{k}_{\|}| = |\vec{k}_0| \sin \theta_a = n\frac{2\pi}{a}. \tag{2.4}$$

As a result of momentum conservation of the electrons we get a quantized change of the parallel momentum

$$\Delta\vec{k}_{\|} = |\vec{k}_0| \sin \theta_a = n\frac{2\pi}{a}. \tag{2.5}$$

Since we are interested in the properties of a surface we also have to take a periodicity orthogonal to the first one in account. Here the lattice spacing is given by b and the angle is θ_b. This leads to the equation

$$\Delta\vec{k}_{\parallel} = |\vec{k}_0| \sin\theta_b = m\frac{2\pi}{b}, \tag{2.6}$$

whereby m is an other integer. To observe diffraction from this surface the last two equations have to be satisfied simultaneously. Now we can introduce a two-dimensional reciprocal lattice vector $\vec{G}$ and we get

$$\vec{G} = \Delta\vec{k}_{\parallel} = n\frac{2\pi}{a} + m\frac{2\pi}{b}. \tag{2.7}$$

The condition for diffraction can also be described by

$$\vec{k}_{\parallel} = \vec{k}^s_{\parallel} \pm \vec{G}. \tag{2.8}$$

Here $\vec{k}^s_{\parallel}$ is the parallel component of k of the scattered electron [2].

A graphical representation of this equation can be obtained by the Ewald sphere construction. In case of a surface, i.e. only a two dimensional lattice, the construction results in a circle instead of a sphere. First we calculate the de Broglie wavelength according to the equation

$$\lambda = \sqrt{\frac{150.6}{E}}. \tag{2.9}$$

Hereby the energy E must be put in eV and the result λ will be in Å. In the next step we can calculate $\vec{k}_0$ according to equation 2.3. Now we draw the reciprocal lattice of the surface and choose one of the lattice points as a center. After that we draw a circle around this point with the radius $|\vec{k}_0|$. The number of reciprocal lattice point inside the circle is equal to the number of diffraction beams which can be observed [2].

As shown in figure 2.4 a LEED apparatus consists of an electron gun, a sample which is grounded to prevent it from charging and four hemispherical concentric grids with a phosphor screen behind them. The electron gun emits monochromatic electrons with a tunable energy E_P in the energy range from 20-1000 eV. With having an inelastic mean free path of 5 to 20 Å these electrons are especially surface sensitive because they can only penetrate the first few monolayers of a solid. The electrons are diffracted by

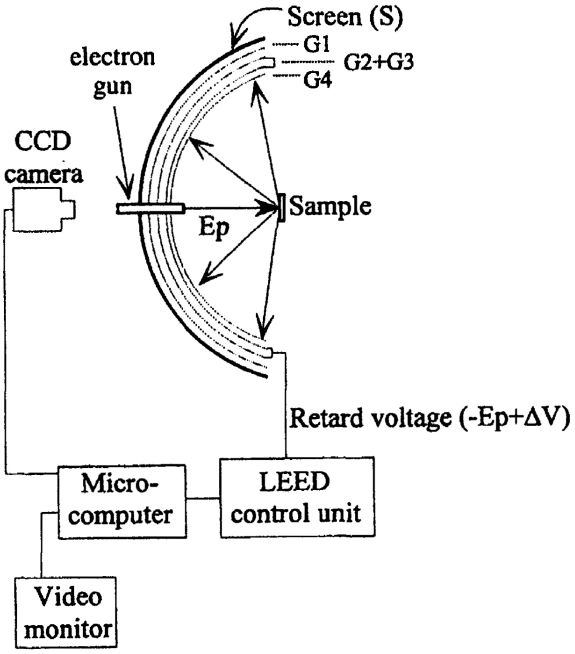

Figure 2.4: Schematic setup for Low Energy Electron Diffraction (taken from [2])

a periodic surface and scatter back and reach the nearest grid G4. To provide a field free region between the sample and the grid G4 they are both connected to ground. The next two grids G3 and G2 are held on a negative potential to prevent inelastically back scattered electrons from passing them. G1 is grounded again and the electrons are accelerated by a high voltage to cause light emission when they hit the phosphor screen. These bright spots on the screen, called LEED pattern, can be seen by eye or be photographed with a digital camera [2].

In our experimental setup we used LEED basically to ensure that our sample surface was long range ordered in the right crystalline orientation. The apparatus is from Physical Electronic Industries and is controlled by PHI 11-020 LEED Electronics.

2.4 Quadrupole Mass Spectrometer

As a Residual Gas Analyzer the model RGA 300 from Stanford Research Systems is used. The mass spectrometer consists mainly of an ionization chamber, a quadrupole

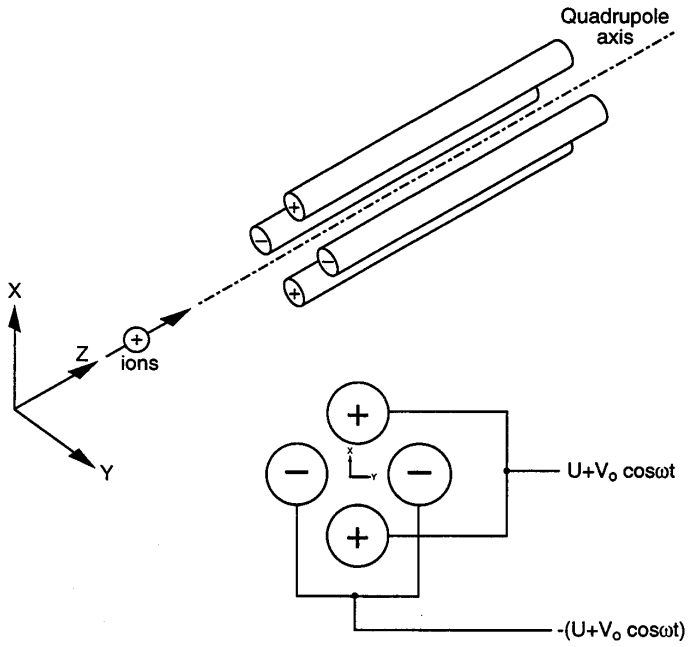

Figure 2.5: Quadrupole mass spectrometer. Ions are produced in ionizer and only the ones with a specific charge-to-mass ration can pass the quadrupole rods and be detected by a Faraday-cup. (taken from [3])

section and an ion detector. Some atoms or molecules of a gas, which has a pressure lower than 10^{-4} Torr, are ionized by electron bombardment. These atoms or molecules can be detected at a partial pressure as low as 10^{-12} Torr. The electrons are emitted from a hot filament and accelerated by a tunable voltage. The resulting positively charged ions are extracted, accelerated and focused into the quadrupole filter. This filter is constructed in a way that only ions with a specific charge-to-mass ratio are allowed to pass it. The filter consists of four stainless steel rods which are set in a rectangular array and isolated by alumina. A schematic view of the this part is given in figure 2.5. An electric quadrupole-field is generated between the rods by applying a D.C voltage U and then superimposing it by a R.F. voltage $V_0 \cos \omega t$. Solving the differential equation describing an ion traveling in this field, the so called Mathieu equation, shows the existence of stable trajectories for every e/m ratio depending on U and $V_0 \cos \omega t$. If the ion does not have the right e/m ratio for the given parameters it collides with one of the rods and it therefore can not reach the detector any more. The ions which pass

the filter are detected by a Faraday-cup. The signal can be amplified by an electron multiplier and then be processed and displayed by a computer [3].

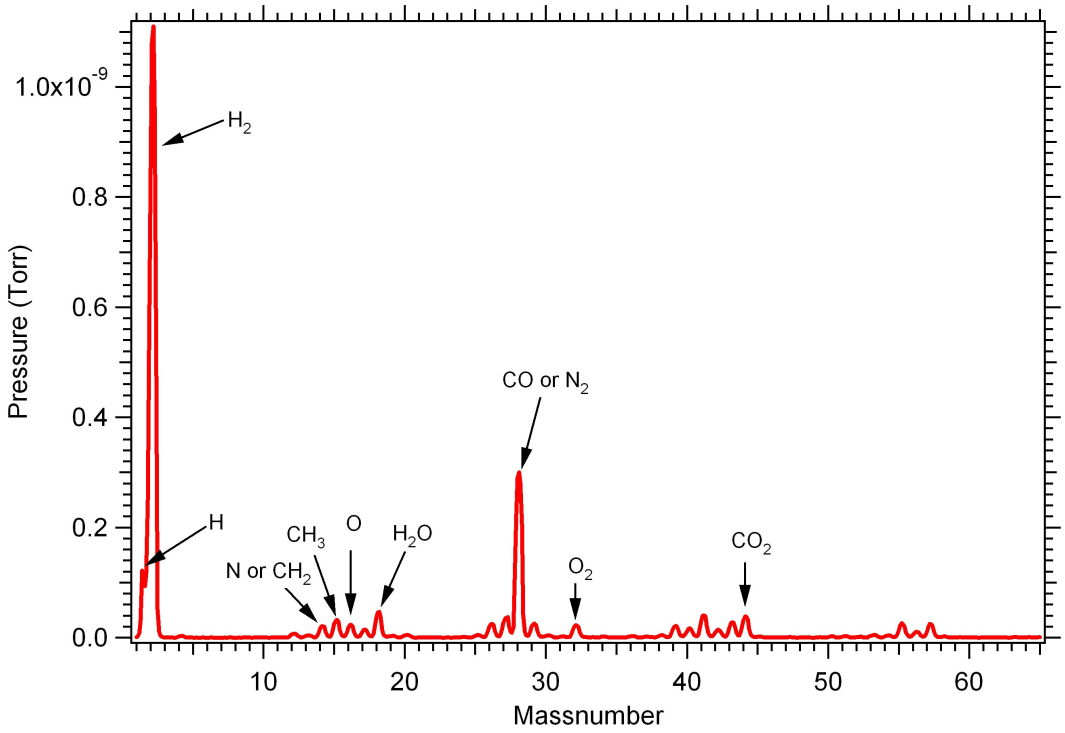

Figure 2.6: Mass spectrum recorded under UHV conditions. The peaks N, CH_3 O_2 and C_2H_6 and the height of the CO or N_2 peak are indications, that there was a leak in the UHV chamber when this spectrum was taken.

Figure 2.6 shows a spectrum which was recorded after pumping and backing the chamber. Under typical UHV conditions huge peaks for H, H_2 at mass numbers of one and two as well as some small ones for H_2O (at mass number 18), CO or N_2 (at mass number 28) and CO_2 (at mass number 44) are always visible. Peaks at a mass number of 14, 15, 16, 30 which corresponds to N or CH_2, CH_3 O and C_2H_6 and the height of the CO peak are indications for a leak.

To find the position of a leak He gas can be used. Parts of the outside of the UHV chamber are exposed to the noble gas. If the He peak at mass number 4 becomes visible it is clear that the He atoms are able to penetrate the chamber walls or sealing in the investigated area. For this purpose the Residual Gas Analyzer RGA 300 offers a mode where only He atoms are detected and their distribution is plotted against time.

2.5 Bayard-Alpert-Gauge

For measuring the pressure in the chamber a Bayard-Alpert-Gauge is used. In this sort of hot cathode ionization gauge electrons are emitted from a filament and then accelerated towards a grid. Thereby the electron ionizes atoms or molecules of the gas in the chamber. The positive ions are detected by a fine collector wire in the middle of the grid to minimize the x-ray limit due to photoemission from the collector, so that the particle density in the chamber can be detected. The operating pressure range is between 10^{-4} and 10^{-10} Torr and this gauge can not be used at a higher pressure because then the filament would be destroyed [12].

2.6 Sputter Ion Gun

In a Sputter Ion Gun a beam of energetic argon-ions is created for sputter cleaning of a sample surface. A hot tungsten filament emits electrons which are accelerated by a voltage of approximately 180 V to ionize the argon atoms. A typical operating pressure range is $5{\cdot}10^{-5}$ to $8{\cdot}10^{-5}$ Torr of argon. The ions are accelerated to an energy of 0.5 to 2 keV, focused to a beam of variable size and hit the grounded target where they sputter the first monolayers of the sample [13].

We use a Physical Electronic Industries Sputter Ion Gun Model 04-131 and the angle between the beam and the surface is 45° to maximize the sputtering effect.

2.7 Turbomolecular Pumps

A turbomolecular pump consists of high-speed rotating blades, the rotator, and fixed blades slotted in the opposite direction, the stator. Figure 2.7 shows a cut through a pump of this type. The system works by compressing gas molecules due to momentum transfer from the fast moving rotating blades. The molecules coming from the inlet are hit by the surface of the blades and gain an additional momentum directed to the outlet. The rotating speed with 24,000 to 80,000 rpm results in tip velocities close to the thermal velocity of air. As a result light molecules like He and H_2, which have a higher thermal velocity, are not pumped as well as heavier molecules. Because the gas

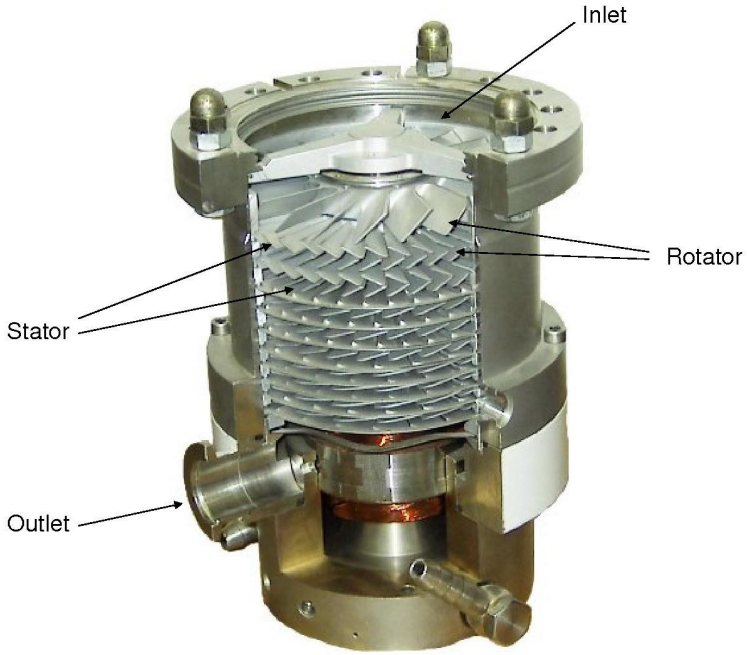

Figure 2.7: Cut trough of a Turbomolecular pump (taken from [4]).

becomes more compressed in the direction to the outlet the stages become smaller and smaller. Ideally the last stage would have been infinity small to pump the gas against atmospheric pressure which can't be realized technically. Therefore a backing rough pump is needed to provide a fore-vacuum. One advantage of turbo pumps is that they don't back stream oil in the chamber themselves. To prevent the back streaming of hydrocarbons from the rough pump both pumps are separated by a valve which closes automatically in case of a power failure [12]. The typical pressure range where the turbo pump can be operated is between 10^{-2} and 10^{-10} Torr [12] even though a starting turbo pump can also pump atmospheric pressure for a short time [14].

In our experimental setup we us a Leybold-Heraeus TURBOVAC 150 with a pumping speed of 145 l/s (for N_2) [14] for pumping the chamber and a Pfeiffer TPU-270 with a pumping speed of 270 l/s (for N_2) [15] for differential pumping.

2.8 Ion Pumps

In an Ion Pump gas molecules are ionized by electrons and then accelerated to the walls of the pump, where they are gettered or buried. When the ions collide with the surface they sputter away the cathode material (in most cases Ti) and create secondary electrons, which are accelerated to approximately 5 keV again. The molecules or atoms are either implanted because of there high kinetic energy when they reach the surface or chemisorbed by the reactive Ti. To enhance the chance that the electrons can hit a molecule even at low pressures they are forced on spiral trajectories by a magnetic field. The Sputter-Ion Pumps have the advantage that they do not contaminate the chamber with hydrocarbons. Unfortunately the diode type, here described, does not pump rare gases well because they do not react with the surface. The typical pressure range for ion pumps is from 10^{-5} to 10^{-11} Torr [12].

2.9 The Ti-Source

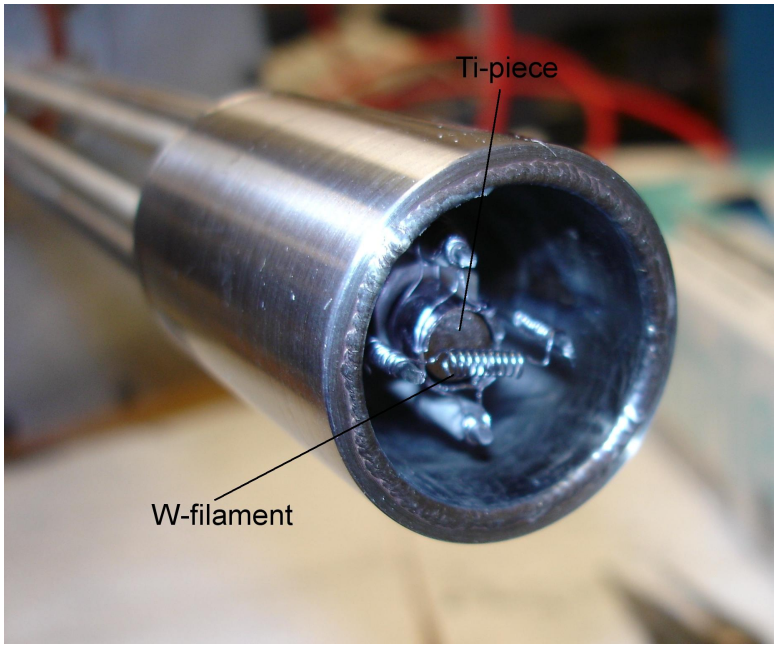

Figure 2.8: The top part of the self-build Ti-source. A hot tungsten filament emits electrons which are accelerated towards a titanium piece where they heat it up until it sublimes and its atoms evaporate from the surface.

Figure 2.8 shows a self-build Ti-source which is used to dope the Al sample with titanium. The source mainly consists of a small titanium block and a W filament. The tungsten filament is heated by a current until it glows and thereby emits electrons. A high voltage is applied between the filament and the titanium to accelerate the electrons so that they can hit the Ti target with a high energy and heat it up. When it reaches its melting point at a temperature of 1668°C some Ti atoms sublimate and evaporate from the surface. These atoms fly through the whole chamber and some of them reach the aluminum sample where they stick to the surface. Because of the high filament temperatures of around 2000°C the outer stainless steel part of the source needs to be cooled with water. To prevent melted Ti from yielding down the wires and creating a short, we constructed a cup of tantalum foil around the Ti piece. Moreover all wires are isolated by ceramics.

The Ti deposition rate can be measured by a water cooled quartz-crystal-monitor which can be moved in front of the source. The deposition of titanium layers on the surface of the quartz alters its vibrational frequency. This change is recorded electronically and showed on a display.

Chapter 3

Fourier Transform Infrared Spectroscopy

3.1 Infrared Spectroscopy and Molecular Vibrations

Infrared Spectroscopy is a widely used technique to investigate vibrations in molecules and to study bindings of atoms and molecules on surfaces. In spectroscopy people look at the interaction of electromagnetic radiation with matter to get information about physical or chemical processes.

In this field it is common to describe the used radiation by wavenumbers $\tilde{\nu}$ in units of cm^{-1} instead wavelengths λ or the frequencies ν. The relations are given by

$$\tilde{\nu} = \frac{1}{\lambda} = \frac{\nu}{c}. \tag{3.1}$$

Hence the energy of the photon can be expressed by

$$E = hc\tilde{\nu} \tag{3.2}$$

where c = $2.99{\cdot}10^{8}$ ms^{-1} is the speed of light in vacuum and h = $6.626{\cdot}10^{-34}$ Js is the Planck constant.

Electronic excitations can be found in the visible ($\tilde{\nu}_{VIS}$= 26,300 to 12,800 cm^{-1}) or ultraviolet ($\tilde{\nu}_{UV}$= 1,000,000 to 26,300cm^{-1}) region of the radiation spectrum while molecular rotations are excited by microwaves ($<$ 33 cm^{-1}). The infrared spectrum is divided in Near- (located at 12,800 to 3,333 cm^{-1}), Mid- (at 3,333 to 333 cm^{-1}) and Far-infrared (at 333 to 33 cm^{-1}). Using the mid-infrared part of the radiation spectrum makes it possible to look at the vibrational bands of molecules [16].

In molecules atoms can vibrate around their equilibrium position with frequencies corresponding to their discreet energy levels. If electromagnetic radiation with the right energy interacts with the molecules then a resonance effect appears and vibrations

are excited. Thus the absorbed frequencies depend on the number and mass of the atoms, the type of the binding between them and also coupling effects. Looking only at two atomic molecules and neglecting the fact that usually vibrations and rotations are coupled makes is much easier to understand some principles of this issue. The molecule can be described as quantum mechanical harmonic oscillator in first or by an anharmoic quantum mechanical oscillator in a better approximation. A good empirical model potential for this oscillator is the Morse potential given by

$$V(x) = D_e(1 - e^{\beta x})^2. \tag{3.3}$$

Hereby D_e describes the depth of the potential well and β describes the curvature at the bottom of the well. From the solution of the quantum mechanic calculations follows for the energy

$$E_\nu = hc\tilde{\nu}(\nu + \frac{1}{2}) + x_e hc\tilde{\nu}(\nu + \frac{1}{2})^2. \tag{3.4}$$

Here ν, the quantum number of the vibration, is not to be confused with the wavenumber $\tilde{\nu}$ and x_e is a anharmonity constant. The quantum mechanic transition rules are given by

$$\Delta\nu = \pm 1, \pm 2, \pm 3... \tag{3.5}$$

where $\Delta\nu = \pm 1$ is called fundamental transition and $\Delta\nu = \pm 2, \pm 3, \pm 4$ are called overtones which appear less likely. Their relative intensities are around [17]

$$1 : x_e : x_e^2 : x_e^3... \tag{3.6}$$

Every molecule consisting out of N atoms shows 3N degrees of freedom of which 3 are for translation in space and 3 are for rotation (2 in case of a linear molecule). This leaves 3N-6 degrees of freedom for vibrations (3N-5 in case of a linear molecule) called normal modes. All the vibrations of a system can be described by a superposition of its normal modes. There are different names for these modes depending on how the molecule is vibrating. If only the lengths of the bondings are altered then the mode is called symmetric or asymmetric stretching mode. The term bonding mode is used if the angle of the bonding is varied. Generally the wavenumbers are higher for stretching than for bonding modes and the asymmetric vibrations show higher frequencies than the

symmetric ones. But this does not necessary mean that always 3N-6 different frequencies can be observed. It is also allowed that some of them are degenerate i.e. they have the same energy. Moreover not every vibration is infrared active because only the ones where the molecule has static or dynamic dipoles can be excited with IR-radiation. Thus the symmetric stretching mode of a molecule without a static dipole can't be seen by IR spectroscopy and only the asymmetric stretching modes and bending modes can be found [17]. Since for molecules bound to surface translation and rotation is forbidden the number of vibrations increases to 3N [16].

3.2 Basics of Fourier Transform Infrared Spectroscopy (FTIR)

In a Fourier Transform Spectrometer a beam of electromagnetic radiation is split into two beams which travel at different optical paths before they recombine again. This recombined beam is used to probe a sample and then recorded by a detector as an interferogram, i.e. intensity distribution over the optical path difference. The Fourier transformation of this interferogram calculated by a computer shows the intensity of the signal in dependence of the wavenumbers, known as the corresponding spectrum. This results in two major advantages compared to conventional grating techniques called Fellget and Jacquinot advantages. First the entire spectral range of the radiation is used during every scan while only a very small region of wavenumbers can be used in the other methods. That is why this benefit is also called multiplex advantage. Second the interferometer has the ability to collect larger amounts of energy at higher resolution than a grating spectrometer which is known as Jacquinot or throughput advantage. This can be explained by the fact that higher amounts of energy can reach the detector due to the lack of instrument slits where the light has to pass through. Moreover large circular sources or entrance apertures can be used without losing resolution as long as the second diffraction order does not reach the interferometer. All this results in a better signal to noise relation [18].

Figure 3.1 shows a picture of the Fourier Transform Spectrometer which was used for this work. The artificially added red line represents the path of the infrared beam. A continuous spectrum of IR light is emitted by a thermal IR-source (1) and focused

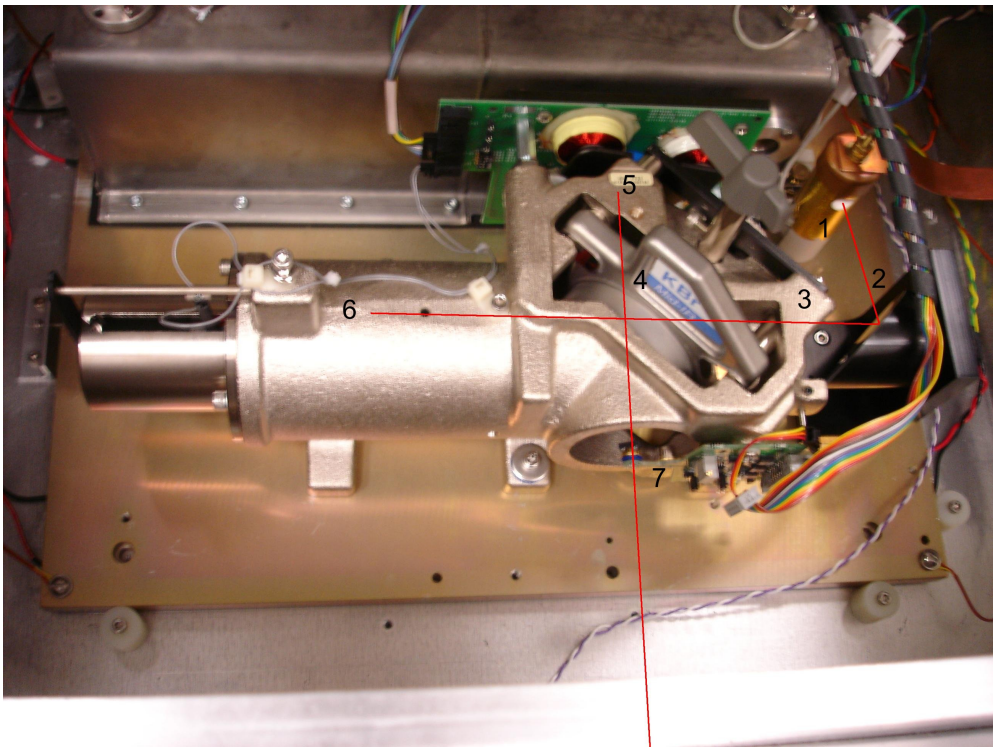

Figure 3.1: Picture of the used Fourier Transform Spectrometer with artificially added IR-beamline.

through a mirror (2) on a aperture (3). Now the beam enters a Michelson-type interferometer consisting out of a beamsplitter (4), a fixed (5) and a movable mirror (6). Because we are using the mid-IR region a KBr beamsplitter is used to divide the beam in two coherent beams with the same intensity. One of them travels to the fixed mirror and is reflected there while the other one is reflected by the moving mirror. Both of the beams recombine at the beamsplitter again and leave the spectrometer. Since the light traveled different ways the resulting beam is now amplitude modulated. This signal can be checked by a small help detector (7).

To control the movement of one of the mirrors and to find the right optical pathway a HeNe-laser is installed in the interferometer. Its monochromatic light travels the same way as the IR radiation. Thus all length measurements and the wavenumbers in the spectrometer can be determined with the accuracy of laser light which makes it a very accurate technique [19]. This feature is known as Connes advantage.

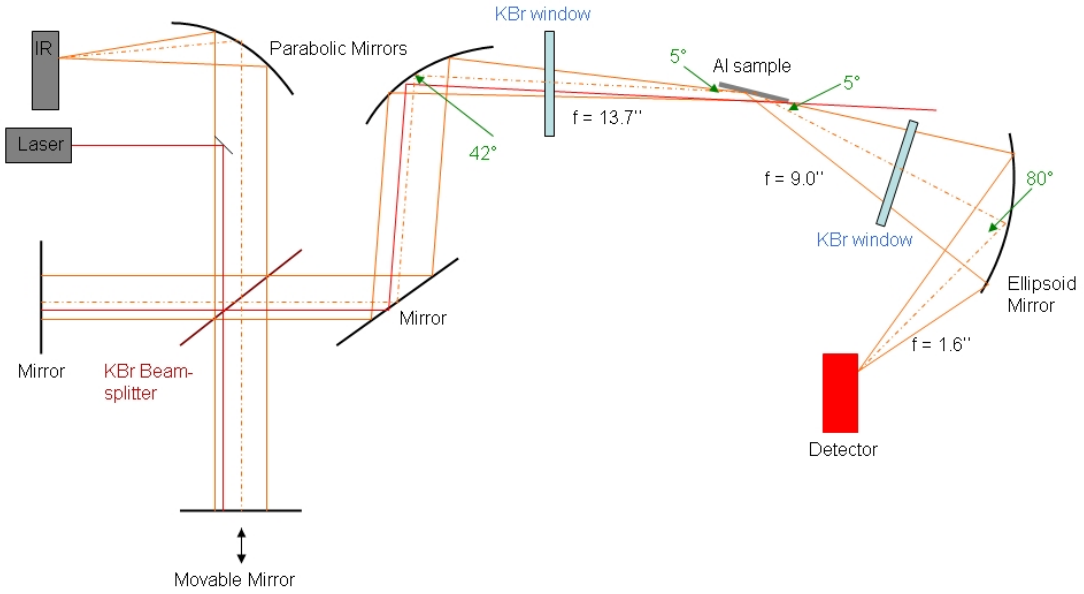

Figure 3.2: Schematic drawing of the optics which were used for the IR- and the laser-beam (not to scale).

A schematic drawing of the beam path together with the used optics can be seen in figure 3.2. When the laser and the IR radiation leave the spectrometer the laser spot is not in the center of the 1 3/8" broad IR-beam. Both beams are reflected by a plane mirror to an off-axis-parabolic mirror. This mirror with a focal distance of 13.7" focuses the radiation on the Al sample. The angle between the incoming and reflected beam at this mirror is 42°. The IR beam travels through the KBr entrance window and hits the Al surface under a grazing incidence angle of about 5°. Unfortunately the laser is not in the center of the IR beam so the laser beam does not hit the sample when the IR reflection has a maximum which makes calibration a lot harder. The IR beam is reflected, leaves the sample under an angle of 5° and travels through a KBr window to an ellipsoid mirror. Here the angle between the incoming and reflecting beam is 80°. This type of mirror has two focus points one at 9.0" and the other at 1.6". Thus it can be used to focus the signal from one of them to the other. Since the first focal distance is much larger the relatively big image size of 3/8" at the Al sample can be focused to a very small spot in the center of the detector.

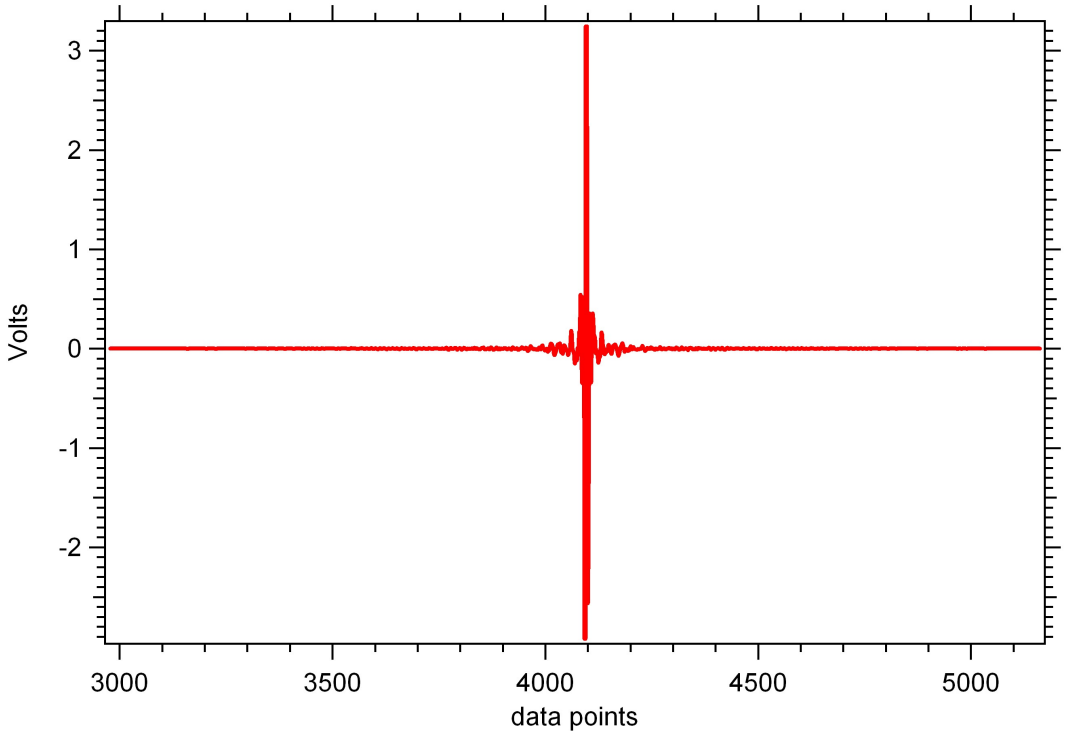

Figure 3.3: A typical interferogram, i.e. intensity distribution over the optical path difference, with the ZPD in the middle.

Figure 3.3 shows a typical interferogram which was collected by the detector. The most striking feature is the huge peak in the middle which corresponds to the point of zero path difference (ZPD). As the name says this is the point of the moving mirror where both beams travel exactly the same distance resulting in a constructive interference for the reunified beam. The setup is the same for a Michelson Interferometer. For every distance Δs the mirror moves away form the ZPD the light has to travel the optical path difference $x = 2\Delta s$ since it has to go to the mirror and back to the beamsplitter. Thus we find constructive interference for

$$x = n\lambda \tag{3.7}$$

and destructive interference for

$$x = n + \frac{1}{2}\lambda \tag{3.8}$$

whereby λ is the wavelength of the used light and n is an integer. This results in a intensity $I_0(x)$ for the interferogram given by

$$I_0(x) = B(\tilde{\nu}_0)[1 + cos(2\pi\tilde{\nu}_0 x)] \tag{3.9}$$

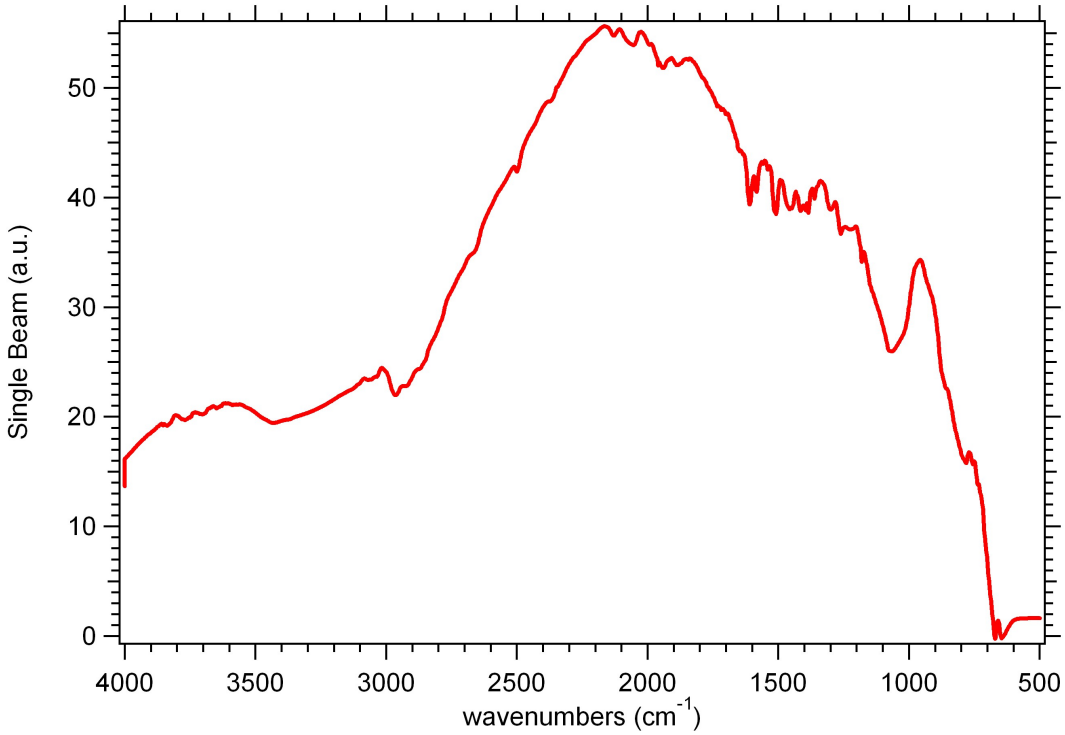

Figure 3.4: The corresponding spectrum to the interferogram shown in figure 3.3.

in the case of monochromatic light [19]. Hereby $B(\tilde{\nu}_0)$ is the intensity for just one wavenumber. Since we are interested in several wavenumbers we have to take a superposition of such single intensities. Moreover we do not care about the mean value of the interferogram so it can be subtracted from the expression. This gives us [19]:

$$I(x) = \int_0^\infty B(\tilde{\nu}) \cos(2\pi\tilde{\nu}x) d\tilde{\nu}. \tag{3.10}$$

To change the limits of the integral the expression above can be written in a complex notation

$$I(x) = \int_{-\infty}^\infty B(\tilde{\nu}) e^{i2\pi\tilde{\nu}x} d\tilde{\nu}. \tag{3.11}$$

Because it is impossible to build a interferometer with a infinite path difference a step function $D(\tilde{\nu})$ has to be introduced to cut off the area outside the used spectral region resulting in

$$I(x) = \int_{-\infty}^\infty B(\tilde{\nu}) D(\tilde{\nu}) e^{i2\pi\tilde{\nu}x} d\tilde{\nu}. \tag{3.12}$$

For analyzing the data we are interested in the spectral distribution $B(\tilde{\nu})$. We can get this spectrum by applying the inverse Fourier transform on the interferogram I(x) which

finally leads to [19]

$$B(\tilde{\nu}) = \int_{-\infty}^{\infty} I(x)D(\tilde{\nu})e^{-i2\pi\tilde{\nu}x}dx. \tag{3.13}$$

This is usually done by a computer using the Cooley-Tukey Fast Fourier Transform algorithm [18]. Figure 3.4 shows the corresponding spectrum to the interferogram in figure 3.3 which was calculated in this way.

3.3 Infrared Reflection Absorption Spectroscopy (IRRAS)

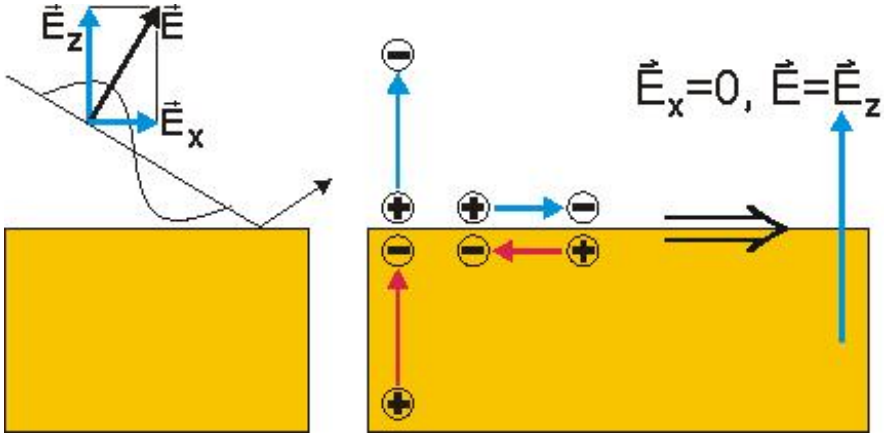

Figure 3.5: An incoming electromagnetic wave can be divided into a perpendicular and parallel component which leads to different polarization effects on the surface of a metal (modified from [5]).

Infrared Reflection Absorption Spectroscopy (IRRAS) is widely used because it is a very sensitive and a non destructive method for investigating surfaces. Hereby an IR-beam is externally reflected by a metal surface. The electrons of the metal are moved by the interaction with the electromagnetic field which leads to a polarization of the surface. Figure 3.5 shows an easily accessible explanation of the effects happening on the surface. The incoming electromagnetic wave can be divided in two components, one parallel and another perpendicular to the surface. The component parallel to the surface moves the electrons in a way that they build up a polarization together with the non-movable ions in the solid. This new electric field is directed opposite to its cause. The superposition of both fields adds up to zero resulting in the fact that the components parallel to the metal surface can not be seen in IR-spectroscopy. The effect for the perpendicular component is different. Here we find that the charge nearest to the surface cancels itself

with its mirror charge leaving the two charges far away from the surface behind. Thus the polarization is enhanced and can be recorded with a spectrometer [5]. This effect can be maximized by increasing the perpendicular component of the beam. That's why a grazing angle of about 5° between the IR beam and the sample is used.

3.4 Fourier Transform Infrared Spectroscopy in our Experiment

In this work a Thermo Nicolet I-Box spectrometer with a KBr-beamsplitter for mid-IR was used. During measurements the interferometer and the whole beam-line outside the chamber is purged with around 10 Torr of pure nitrogen. This makes it possible to provide a stable environment and to minimize CO_2 and H_2O contaminations of the signal.

Different types of IR-detectors can be installed outside the UHV-chamber. All detector types show a different recording behavior and therefore have a maximal signal in a special spectral range. For the wavenumber area between 400 and 4000 cm^{-1} a Deuterated Triglycine Sulfate (DTGS) photoconductor is the system of choice while in the region from 800 to 4000 cm^{-1} a Mercury Cadmium Telluride (MCT) detector can be used. The advantage of a MCT detector is that it is faster and reaches a higher detectivity but it has the drawback that it has to be cooled down with liquid nitrogen. This makes it impossible to operate it for long measurement times when the liquid N_2 can not be refilled. Moreover an InSb photovoltaic detector with the range from 1800 to 5000 cm^{-1} was used for test purposes. This type of detector also has to be cooled down.

The signal of the detector is amplified and then recorded by a computer using the OMNIC software from Thermo Nicolet. All our spectra were obtained with a resolution of 4 cm^{-1}. Usually 1000 scans were averaged to one spectrum to obtain a good signal to noise ratio at a reasonable scanning time.

At least one IR-spectrum is taken as a reference before the experiment starts. Then other spectra of the modified sample are recorded, called the signal. To calculate the

absorbance $A(\nu)$ the equation

$$A(\nu) = -log\left(\frac{I_s(\nu)}{I_r(\nu)}\right) \tag{3.14}$$

is used, were $I_s(\nu)$ is the intensity of IR radiation as a function of the wavenumber for the signal and $I_r(\nu)$ the corresponding value for the reference. This absorbance contains the physical interesting information on the layer vibrational modes. A baseline correction for the data can be made using the OMNIC program if necessary. Hereby a background is subtracted from the absorbance to remove slopes which are caused by changes due to fluctuations in the position or temperature of the sample or the detector.

Chapter 4

Sample Preparation

4.1 Cleaning the Sample

For the whole experiment it is important to have a clean Al surface without contaminations by other elements. Aluminum forms an oxidation layer very easily when it is exposed to oxygen. This also happens under UHV conditions after a certain time. Thus it is necessary to clean the sample every time before working with it.

As described earlier we are using a Sputter Ion Gun and Ar-sputtering to remove the topmost monolayers of the contaminated sample. During sputtering the chamber is filled with Ar-atoms at a pressure of $7.0 \cdot 10^{-5}$ Torr. Since the sample is with a surface size of 2.5 $\times$ 1 cm relatively big we have to move it in order to scan the whole surface with the Ar-beam. This makes the process more difficult and time intensive. The typical cleaning cycle consist of 32 min argon sputtering while the location of the incident beam on the sample is changed by 1 mm every 4 min. A total of eight changes is necessary to clean one part of the sample. Usually three of these cycles are necessary per day to maintain a clean surface. One of them is performed on the top, one in the middle and one at the bottom of the sample. The kinetic energy of the ions is kept at 0.5 keV and the temperature of the sample is slowly raised to 230°C. After this step the chamber is pumped down to a pressure range of 10^{-9} to 10^{-10} Torr and we anneal the sample to a temperature of 400°C. The high temperature facilitates the desorption of contaminating atoms or molecules and gives the Al surface the energy to geometrically order.

If the sample is exposed to air at atmospheric pressure the aluminum oxide layer is thicker and quite hard to remove. In this case it takes weeks of cleaning to regain a clean sample. To speed up the process we start with a higher beam energy of 1 keV and

reduce it to 0.5 keV as soon as the surface becomes cleaner, which is quantified using AES.

4.2 Checking the Cleanliness of the Sample

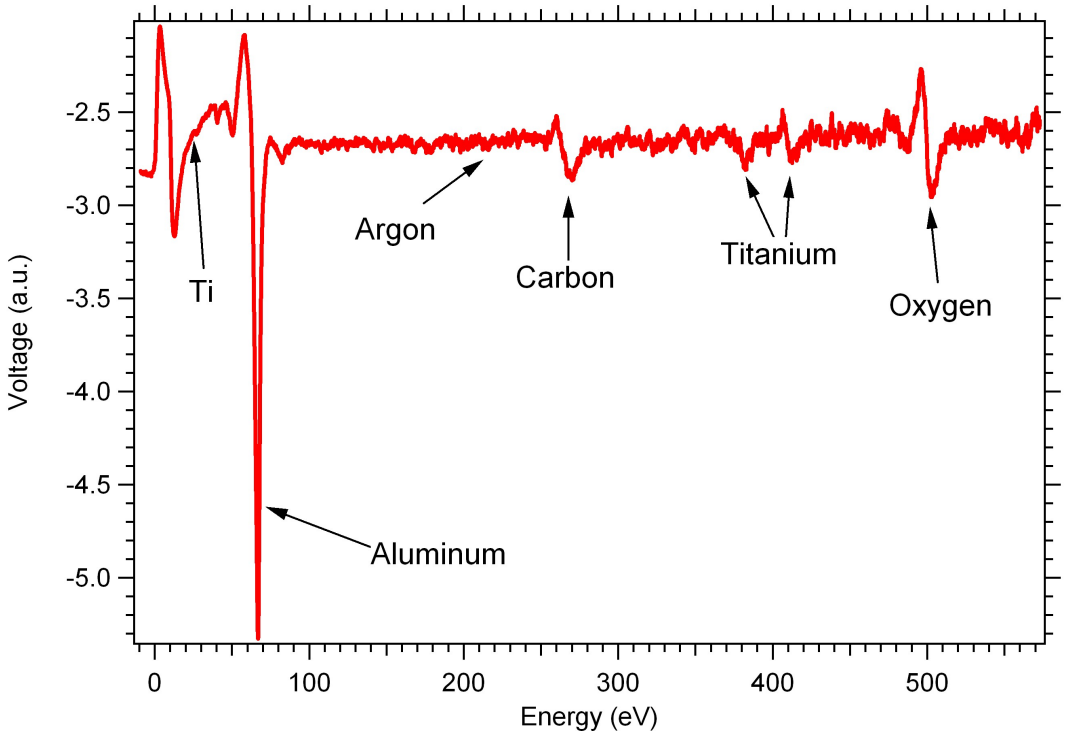

Figure 4.1: Typical AES of Al(111) before the cleaning processes. The main contaminations O, C and Ti are clearly visible in this spectrum while the intensity of the Ar peak is very week.

For checking the cleanliness of the surface we use Auger Electron Spectroscopy (AES). Figure 4.1 shows a spectrum of a contaminated Al surface. The main contaminations are usually O (at 503eV) and C (at 272 eV), with Ar (at 215 eV) and Ti (28, 387 and 418 eV) after some sputtering and Ti depositions. It takes a couple of sputtering/annealing cycles to remove them completely. The progress of the cleaning can be seen in figure 4.2. The topmost spectrum shows the contaminations which stick to the surface when the sample was not cleaned during a weekend. The second spectrum was recorded after three sputtering cycles at 1 keV and room temperature. Apparently the oxygen peak decreases visibly while the carbon peak only vanishes slowly. Moreover a new Ar-peak grows since the Ar atoms from the sputtering are incorporated into the

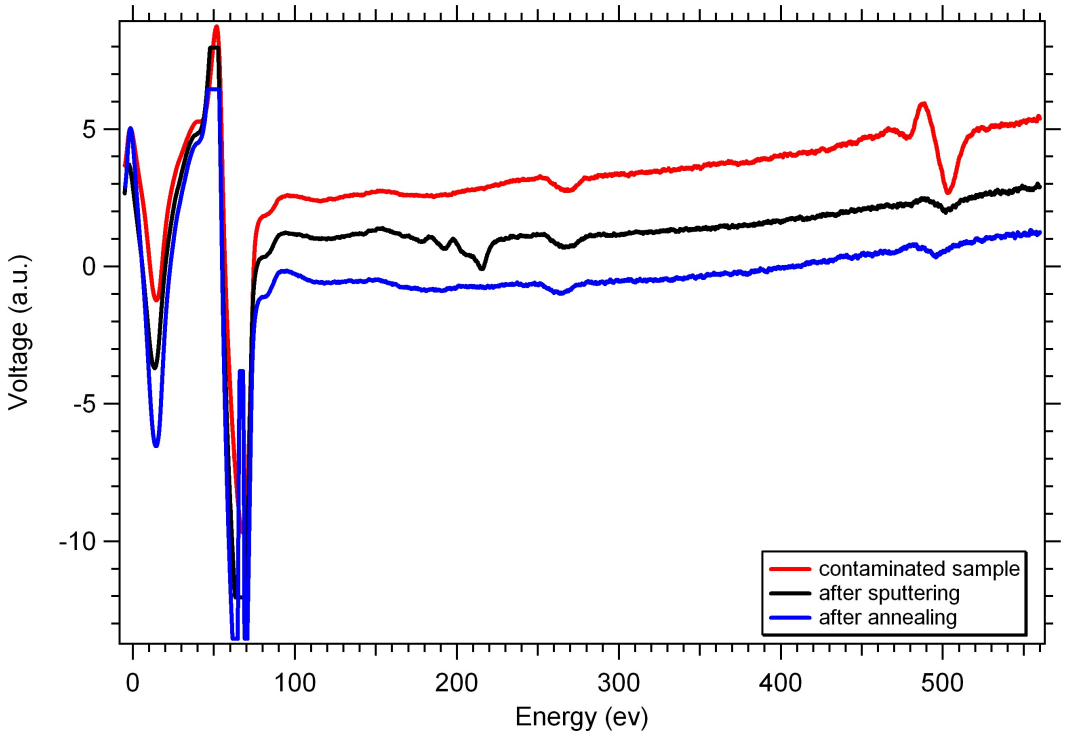

Figure 4.2: Auger spectra before, after sputtering and after annealing. An amplification of 20 was used to record these spectra.

near surface region. After this step the sample is annealed to 400°C to get rid of the argon atoms and to minimize the other contaminations. This cleaned surface is finally represented by the spectrum on the bottom. The Al augerline is partially obstructed due to the restricted voltage range of the PCI card in the computer. Only amplitudes with $\pm$ 10 volts can be recorded by our A/D converter and after that the signal is cut off.

For all measurements the differential mode dN/dE is used because it makes it easier to identify the representative peaks for the elements. The electron bombardment from the AES causes a current in the sample. Typically we try to reach a current of 4 μA to be able to compare different spectra. Moreover we can choose different amplifications of the signal depending on the size of the features. In figure 4.1 no amplification is used while in figure 4.2 the maximal factor $\times$20 is shown.

The surface suffers significant damage because of the bombardment with Ar-ions. To make sure that the surface has a long range order after annealing and to confirm that

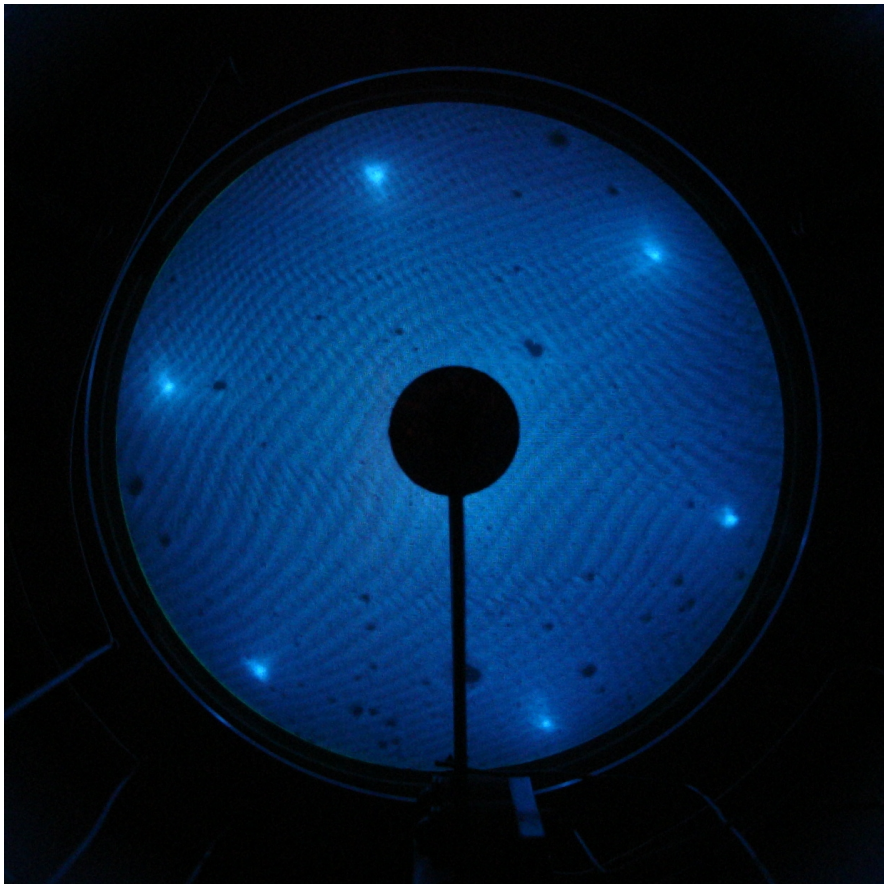

Figure 4.3: Leedpattern of a clean Al(111) surface recorded at an energy of 53.5 eV. The hexagonal symmetry certifies that the probed sample shows a closed packed surface as expected for Al(111).

we still look at the right crystalline orientation, we use Low Energy Electron Diffraction (LEED). As shown in figure 4.3 we are able to record an hexagonal LEED pattern for a hexagonal closed packed surface like on Al(111) when the sample is clean.

Chapter 5

Hydrogen on Al(111)

5.1 Introduction

In the first part of the experimental work the hydrogen adsorption on a clean aluminum(111) surface was investigated. Since aluminum has a face centered cubic (fcc) lattice structure its (111) surface is closed packed, i.e. it is atomically smooth with the maximal amount of atoms per layer [2]. Thus the surface of the single crystal which was used for the measurements consists mainly of (111)-terraces with some atomic close packed steps between them [6]. Our research efforts start with pure Al since it is relatively easy to deal with from a theoretical point of view. A simple description of its electronic structure can be given by a free-electron model [20].

It is well known that molecular hydrogen does not adsorb on a Al surface at room temperature and only atomic hydrogen sticks to the surface [21]. This atomic hydrogen etches the surface and forms aluminum hydrides, called alanes (AlH_3, Al_2H_6 etc.). We will see that this formation occurs on step-edges and on terraces. Go et al. [6] first imaged alanes on an Al-surface using a scanning tunneling microscope (STM). Figure 5.1 shows one of their STM pictures. The alanes are represented by small bright protrusions on darker Al(111)-terraces of different heights. The step-edges appear to be randomly etched by the hydrogen.

More evidence for alane formation on aluminum surfaces is its desorption behavior around room temperature. It was reported [21] that up to 50% of H adsorbed to an Al(111) surface was desorbed in form of aluminum hydrides.

Because of the complexity of this whole process and many unanswered questions concerning the formation of the alanes we investigate this system with IR-spectroscopy.

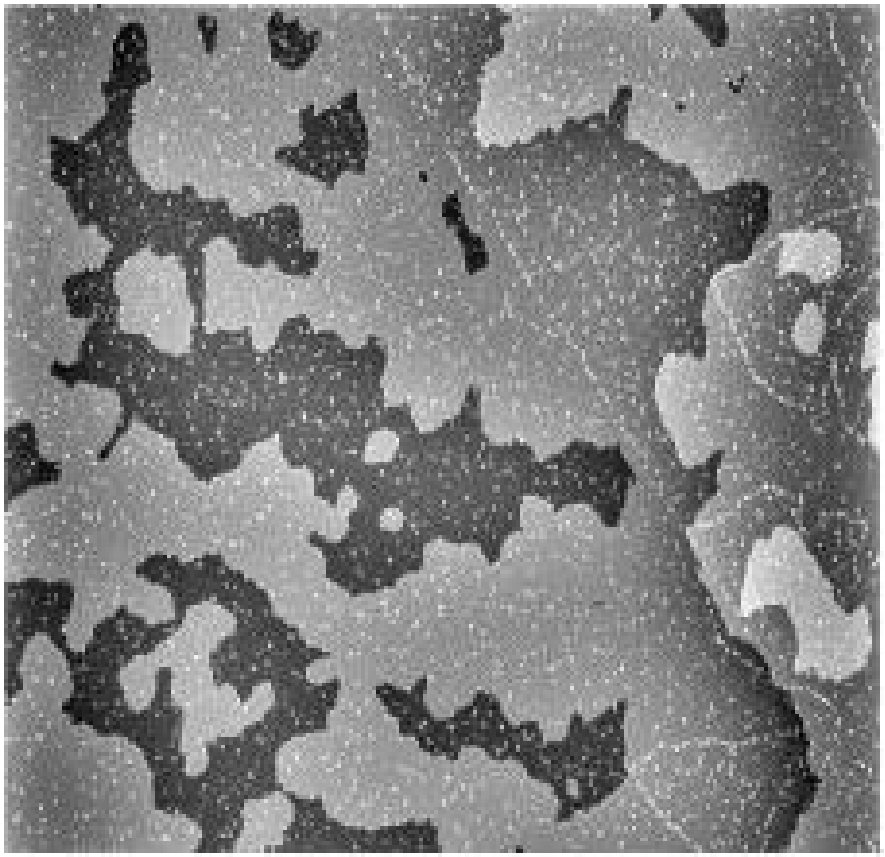

Figure 5.1: STM picture of alanes (white spots) on a now etched Al(111) surface. The total width of the surface part shown in the picture is 5000 Å (taken from [6]).

Moreover little is known about the mass transport on the surface. We need information about the Al-H interaction to see the changes when the surface is doped with a Ti-catalyst in a later step of the project.

5.2 Experimental Procedure

The sample is cooled down to 93 K using liquid nitrogen and a single beam spectrum of the pure Al surface is recorded to be used as a reference. Then the UHV-chamber is filled with molecular hydrogen at a pressure of $1{\cdot}10^{-6}$ Torr. A hot tungsten filament dissociates H_2. A temperature of 2000K is chosen because this is hot enough to dissociate hydrogen but still under the evaporation temperature of W. Since it is impossible to determine the exact amount of H reaching our sample we measure the time when the wire is hot enough to dissociate hydrogen. We express the dose of H on the surface by

Langmuir (L). The definition of one Langmuir is $1{\cdot}10^{-6}$ Torr s [22]. The actual amount of atomic hydrogen which reaches the surface depends on the solid angle between the filament and the sample and on the distance between them because H can recombine to H_2. Moreover the size and the temperature of the filaments determine the amount of atomic hydrogen which is created. During an adsorption process the crystal temperature increases by around 10K. Usually the IR-spectra are taken during and after each exposure. Then the absorbance is calculated following equation 3.14 and a baseline correction is made if necessary. The spectral range which is most interesting for our studies lies between 2000 and 1400 cm^{-1}. The modes below 1400 cm^{-1} are not visible with our detector.

5.3 Results and Discussion

5.3.1 Low Hydrogen Exposures at 93K

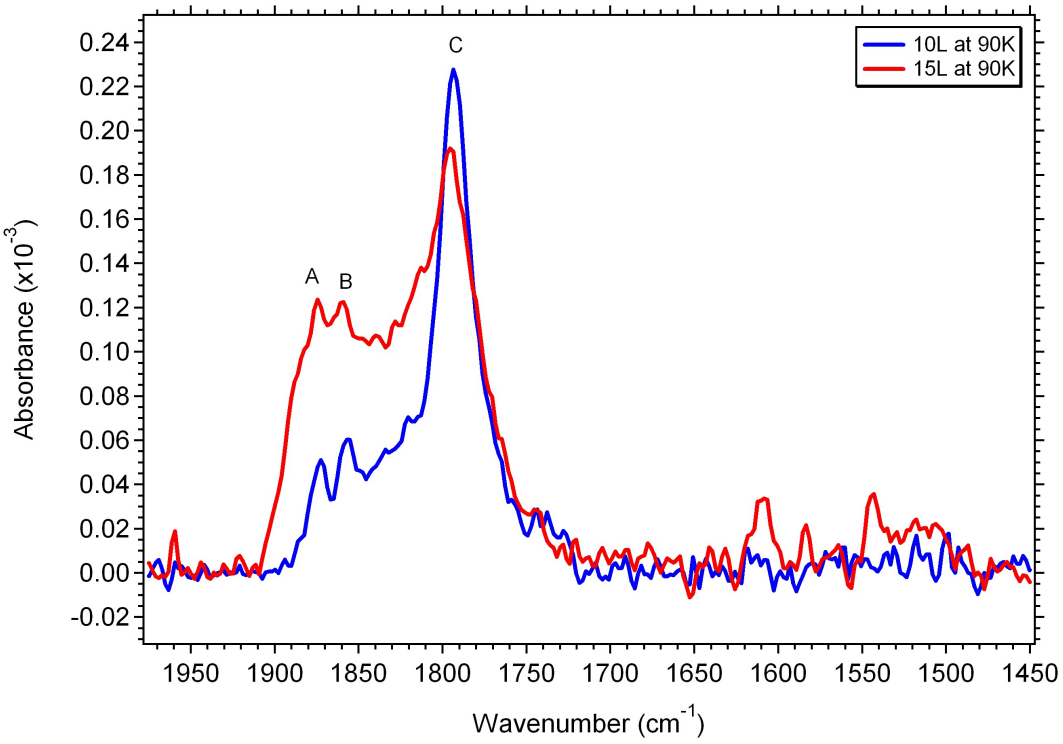

Figure 5.2: Two low hydrogen exposures at 93K. The peak C around 1790 cm^{-1} corresponds to adsorbed H on step-edges while the peaks at 1875 and 1860 cm^{-1} are terminal stretching bands of H bond to alanes (A) and Al (B).

Figure 5.2 shows two low hydrogen exposures one at 10L and the other at 15L recorded at a temperature of 93K. Thereby the spectra were taken after the exposure and averaged over a time of 10 min. The discussion will focus on the evolution of the three main features at 1875 (A), 1860 (B) and 1790 cm^{-1}(C). Two of them have been identified by Go et. al. [6] as stretching vibrations of H on step edges (C) and the stretching vibrations of terminal H in the monomer AlH_3 when it lies on terraces (A). The third one (B) at $\nu_{T(H)}$= 1860 cm^{-1} corresponds most likely to the stretching mode of H which is bonded to the Al(111) terrace. This last feature is only visible at very low H exposures.

For the 10L exposure the highest peak C, which represents H on step edges, occurs at 1790 cm^{-1}. The terminal H atoms bound to the terrace (B) show the second highest feature. The alane terminal H peak A at 1875 cm^{-1} is even less intense.

The main peak C shrinks when the H dose is increased to 15L but the peak A grows and has a much higher intensity than before. This time the feature associated with terminal H of alanes is higher than the one of terminal H on the Al surface. Moreover some new bands appear in the region of 1500 to 1650 cm^{-1}. These are indications that the quantity of small alanes like AlH_3 increases with increasing H dosing to 15L.

A hydrogen exposure of 60L at a temperature of 93K is shown in figure 5.3. This time the dominant peak (A) can be found at 1875 cm^{-1} indicating that the number of small alanes is much higher now. It is followed by a smaller peak corresponding to terminal hydrogen atoms on terraces (B at 1860 cm^{-1}) and an even smaller one at step-edges (C at 1790 cm^{-1}). Thus compared to the lower exposures in Fig 5.2 the intensity of these three main peaks is reversed. Beside these sharp features the broader bands, which are associated with aluminum hydride [6], become more and more visible. According to theoretical calculations done by Santanu Chaudhuri [23] some bridging vibrational bands of alane dimers and trimers lie in the wavenumber region 1470 and 1750. New features appear between 1550 and 1600 cm^{-1} (E) as well as between 1640 and 1760 cm^{-1} (D).

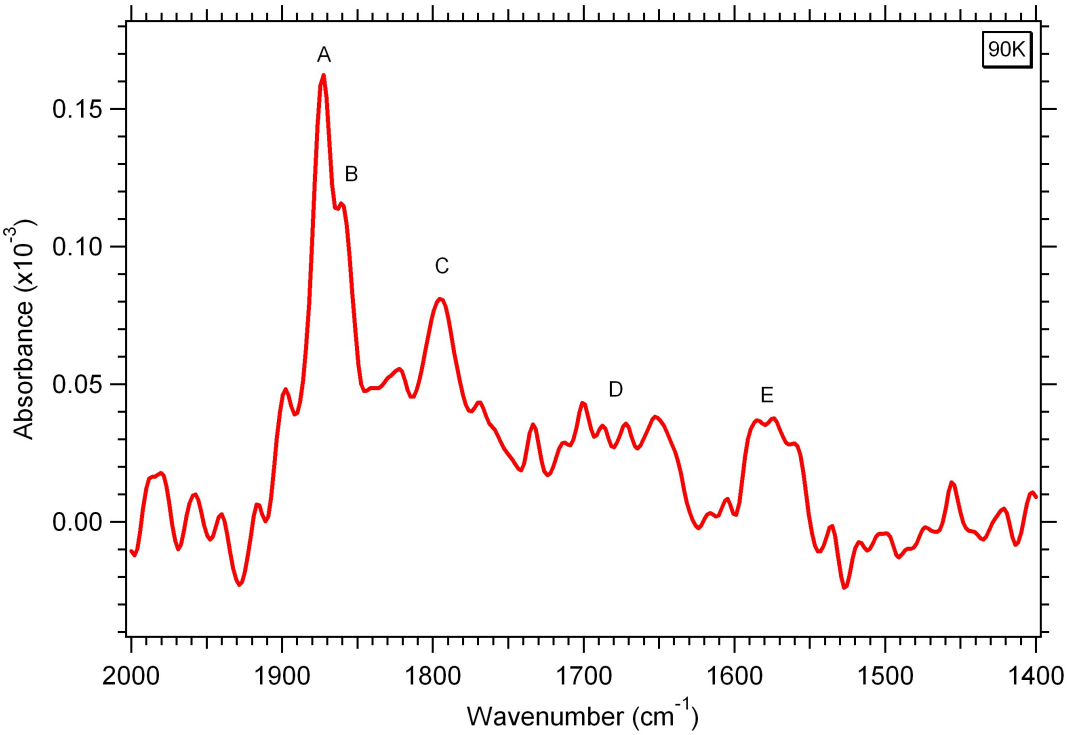

Figure 5.3: A hydrogen exposure of 60L at 93K. The main peak A at 1875 cm^{-1} results form alanes on terraces. Furthermore there are some new structures growing at 1550 to 1600 cm^{-1} (E) and 1640 to 1760 cm^{-1} (D).

5.3.2 Different Hydrogen Exposures at 93K

In another experiment spectra for exposures between 60L and 720L were recorded (see Fig. 5.4) to investigate the changes of the line shapes and to find the saturation value for H adsorption on the surface. Each spectrum is an average over one minute taken during the exposure, i.e. when the chamber was filled with H at a pressure of $1{\cdot}10^{-6}$Torr and the filament was on. The temperature of the sample was again 93K.

The situation for 60L is the same as described above. The dominant peak A at 1873 cm^{-1} corresponds to terminal H-band of small alanes, while the smaller peak B on the right to it describes ad-H on terraces. There is also some hydrogen on step-edges (C) visible at wavenumbers around 1795 cm^{-1}.

When the exposure is doubled, A increases and B stays almost constant. The feature C decreases slowly and finally vanishes. This trend goes on until an exposure of 180L where the B mode also vanishes. Moreover the main peak broadens which might be

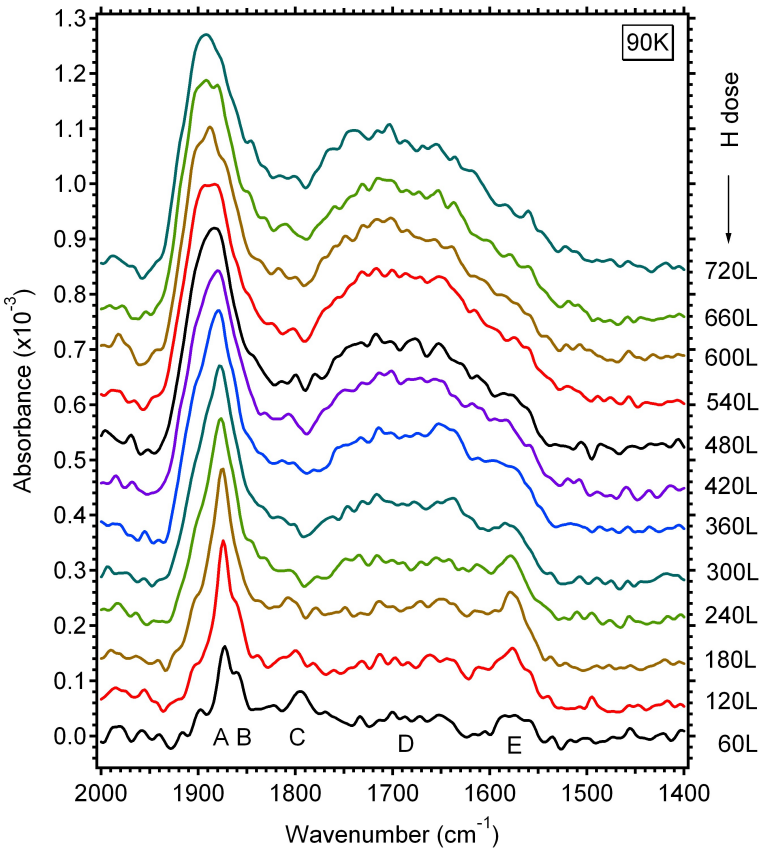

Figure 5.4: Different hydrogen exposures at 93K. For higher H doses there are indications for the formation of bigger alanes.

connected to slightly different vibrational modes of the terminal H-band for alanes of different sizes. During this process the maximum of this band is slightly shifted to higher wavenumbers.

We can also observe a change in the wavenumber region between 1800 and 1550 cm^{-1}. New broad vibrational bands emerge in this area which are attributed to the formation of larger alanes (like Al_2H_6, Al_3H_9 etc.) located on terraces. The scissor modes of adsorbed water also lie in this region, but the H_2 we use for the experiment is very pure (99.9995%) and long term measurements show no indications for an increased adsorption of water on the surface. The peak E between 1550 and 1580 cm^{-1} dominates this part of the spectrum up to a hydrogen dose of 300L. Beyond that dose the broad band D between 1640 and 1760 cm^{-1} grows in intensity before reaching saturation. Some of these bands might be associated with the alane dimer. Theoretical calculations

[23] indicate, that in the case of Al_2H_6 the molecule can also lie parallel to the surface. In this case its bridging modes are not visible for IR-spectroscopy. They can only be detected if the molecule stands up and thereby forms an angle with the surface. The theory also predicts a higher activation barrier for a horizontal Al_2H_3 cluster and therefore this cluster will most likely form at a higher hydrogen pressure.

At a coverage of 540L saturation is reached and the shape of the spectrum does not change significantly anymore. The main feature is now a broader peak A of terminal H atoms bound to different sizes of alanes followed by a even broader region D associated with the bridging modes of those alane clusters.

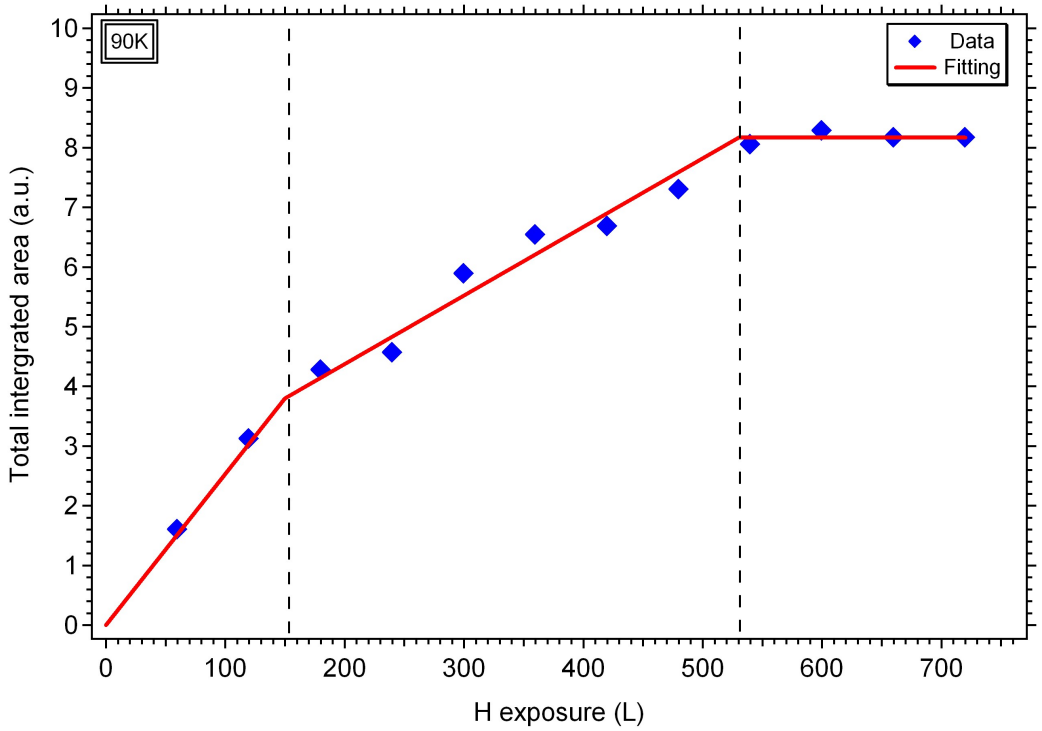

Figure 5.5: Integrated area from 2000 to 1400 cm^{-1} of the spectra after different H exposures. The hydrogenation can be described by a three step model.

Figure 5.5 shows the total integrated area (integrated from 2000 to 1400 cm^{-1}) of the spectra during the different exposures. A linear fit for the data results in a model for hydrogenation connected to the observations made above. We can divide the process mainly in three steps: For low exposures we find ad-H on terraces and step-edges together with formation of AlH_3. As soon as the H dose is higher than 180L the

formation of larger alanes is favored. Finally at an exposure of around 540L saturation is reached and no more hydrogen can be adsorbed on the surface.

5.3.3 Hydrogen Exposures at 250K

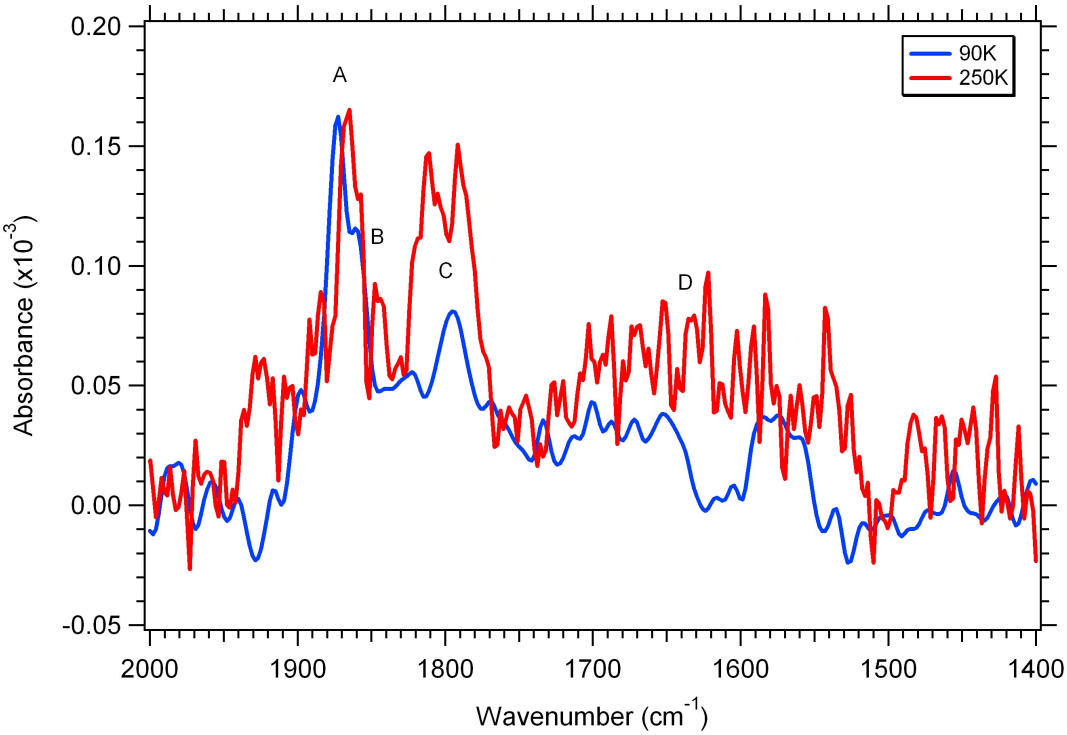

Figure 5.6: Comparison of spectra of a 60L hydrogen exposure at 90 and 250K.

In the preceding section all hydrogen exposures were performed at liquid nitrogen temperature. Since the Al atoms can migrate at room temperature it is interesting to perform experiments as a function of temperature. Now follows the discussion of spectra taken after H exposure at a temperature of 250K.

A comparison between the spectra of a 60L hydrogen exposure at 90K and 250K is given in figure 5.6. Even though both both times the sample was exposed to the same amount of H the spectra show a different behavior.

For both spectra the highest peak A can be found around 1870 cm^{-1}. This feature is associated with the stretching bands of H atoms in the alanes or H bound directly to the terrace. For 250K this peak is a little bit shifted to smaller wavenumbers. The main difference follows in the region around 1790 cm^{-1}. Instead of the single C peak in case

of the low temperature a double peak occurs for the higher temperature experiment. The maxima of this much more intense double peak are at 1810 and 1790 cm^{-1}. Beside these peaks, smaller new peaks can be found in the region between 1910 to 1930 cm^{-1} and around 1850 cm^{-1}. These observations also suggest the formation of larger alane clusters.

The spectral region below 1750 cm^{-1} also looks different. For 250K exposures one broad feature *D* covers the whole area from 1500 to 1750 cm^{-1}. This is similar to what was observed in the case of higher H-exposures at 90K (see Fig. 5.4). Thus it confirms the presence of bigger alanes even at this low coverage.

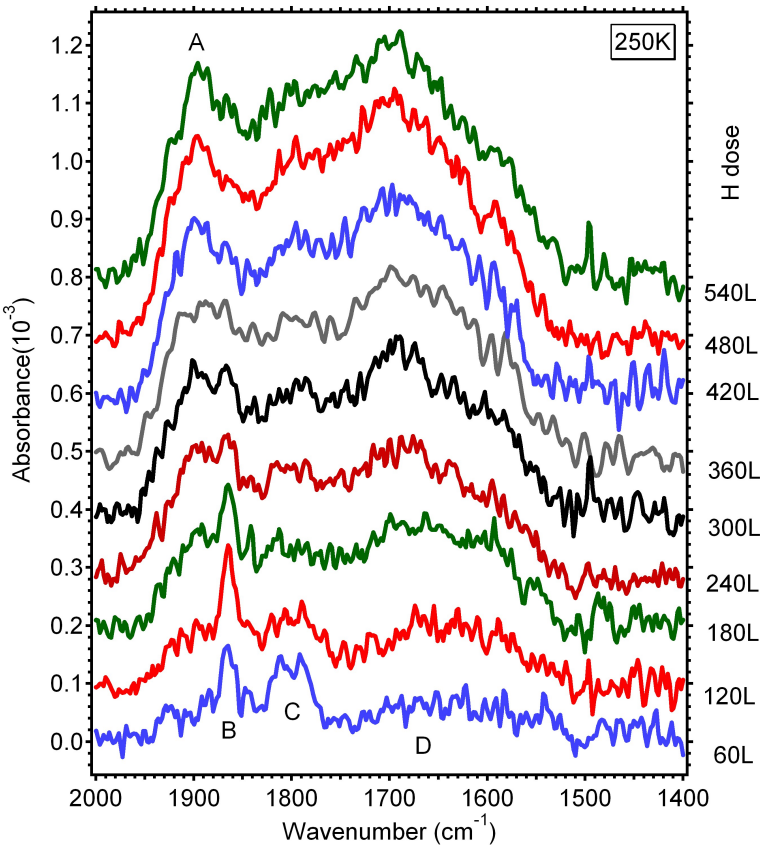

Figure 5.7: Spectra of different hydrogen exposures at 250K.

To investigate the behavior of the hydrogen adsorption at 250K spectra were taken during an exposure from 60L to 540L (figure 5.7). Again each spectrum represents the average over one minute.

The spectrum for 60L is the same as described above. For the exposure of 120L the highest peak B at 1865 cm^{-1} grows and narrows while the peak (C) broadens and looses intensity. The feature D between 1750 and 1500 cm^{-1} stays almost constant.

With increasing H dose, the band A in the wavenumber region from 1870 to 1920 cm^{-1} is becoming more and more intense. This band is most likely related to terminal H atoms on bigger alanes. At an exposure of around 300L it reaches the same height as the peak B. For doses over 360L these vibrational bands grow even more and dominate the peak B.

There are changes also in the spectral region below 1850 cm^{-1}. For example the height of the peak C from 1830 to 1760 cm^{-1} is decreasing. At the same time the feature D between 1750 and 1550 cm^{-1} is growing and its maximum is shifted to higher wavenumbers. For exposures higher than 300L it becomes the most intense feature. As mentioned above the bridging modes of bigger alanes lie in this wavenumber region.

At an exposure of 420L saturation is reached. The maximum of the peak A at around 1900 cm^{-1} is followed by a broader band C between 1770 and 1840 cm^{-1} and finally a broad feature (D) forms between 1550 and 1760 cm^{-1}. This last vibrational band is dominated by a peak located at around 1700 cm^{-1}.

The conclusion is that, in the comparison to exposures of 90K, saturation is reached earlier and it seems that the formation of larger alanes is favored at higher temperatures.

5.3.4 Hydrogen Exposure at 180K

The experiments for different hydrogen exposures were repeated at a temperature of 180K. Each spectrum represents the average over one minute of measurement time during the exposure. The resulting spectra are shown in figure 5.8.

The first exposure was 60L. Again the higher frequency region of the spectrum is dominated by a narrow peak B at 1860 cm^{-1} which is most likely related to stretching modes of terminal H atoms in small alanes. This peak is followed by a double peak (C) with maxima at 1795 and 1810 cm^{-1}. For smaller wavenumbers a broad features D from 1770 to 1520 cm^{-1} can be observed. Because of stability concerns with the detector no reliable statements can be made for the wavenummber region below 1520cm^{-1}.

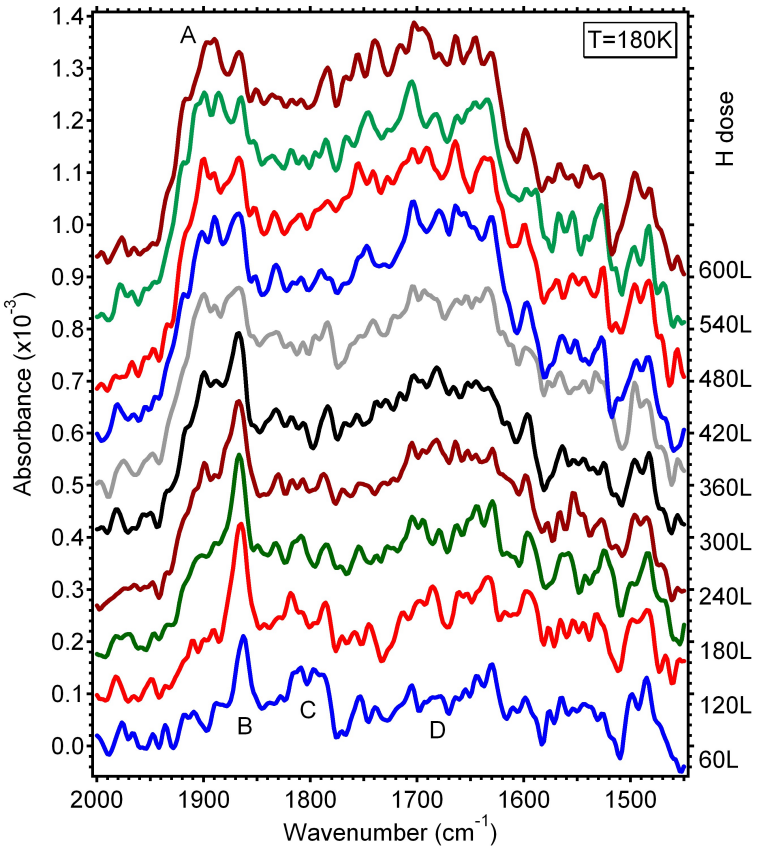

Figure 5.8: Spectra of different hydrogen exposures at 180K.

An evolution of the spectra similar to the one at 250K can be observed. With higher exposures two new peaks (A) at 1890 and 1900 cm^{-1} start to grow and all together form a bigger feature. The three maxima of this feature reach a comparable intensity at a H dose of 360L. Like in the case of 250K these peaks are associated with the stretching modes of terminal H of bigger alane clusters. The double peak C vanishes with hydrogen exposures higher than 180L. Again the broad vibrational bands D between 1770 and 1520 cm^{-1} grow with increasing H dose and shift to higher frequencies as their intensity saturates.

Saturation is reached at an exposure of 480L. The main difference of this spectrum compared to the one at 250 K is that parts of the narrow peak B at 1860 cm^{-1} are still clearly visible.

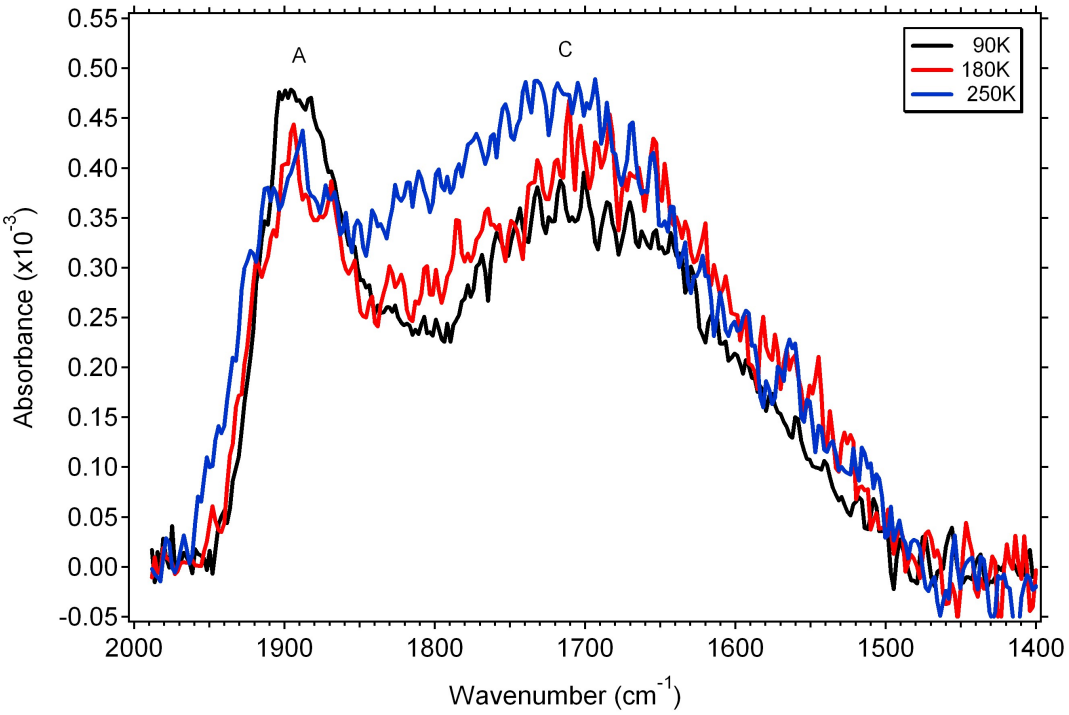

Figure 5.9: Spectra of a saturated Al surface after H-adsorption at 93K (540L), 180K (480L) and 250K (420L).

5.3.5 Saturation for Hydrogen Adsorption at Different Temperatures

Figure 5.9 summarizes the absorption spectrum of a H-saturated Al(111) surface achieved by exposures at three different temperatures: 93, 180 and 250K. It can be seen that the peak A related to terminal H of alanes is the highest for the coldest surface. The corresponding feature shrinks with increasing temperature. The broad band D of the bridging vibrational modes is higher at higher temperatures. Thus we can conclude that the formation of larger alanes is favored at higher temperatures. A possible explanation is that small alanes, which are created first, can diffuse on the surface and when they hit another alane they form bigger clusters. In case of higher temperatures they gain more thermal energy and can thereby diffuse faster and further on the surface. Thus the change of hitting each other is increased.

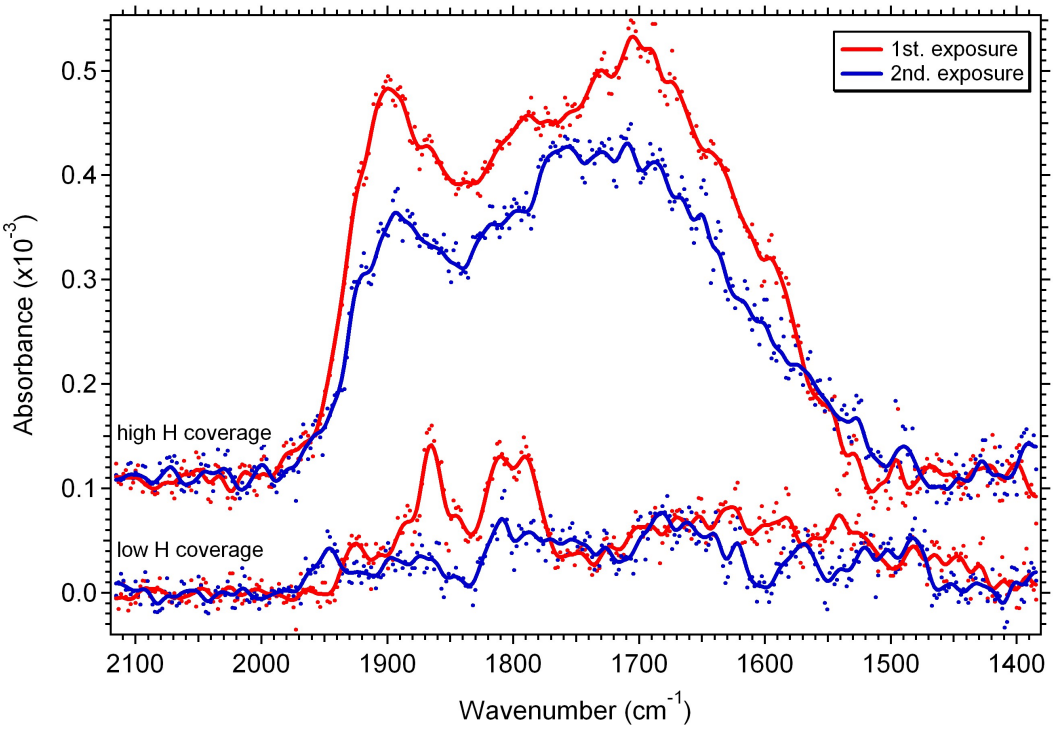

Figure 5.10: Hydrogen exposures and re-exposures after H desorption for low and saturation coverage. Apparently the alane formation is reduced by increasing surface roughness.

5.3.6 Effects of Surface Roughness on Alane Formation.

For this experiment the Al surface was pre-exposed to a small dose of hydrogen. After taking the spectra the hydrogen and the alanes were desorbed by heating the sample to 320K. In the next step the uncleaned and rougher surface was exposed to the same dose of H and a spectrum was taken.

The lower part of figure 5.10 shows the results. The first exposure is represented by the red curve and the second exposure by the blue curve. Both curves were smoothed and the dots display the measured data points. In case of the first exposure a peak at around 1970 and a double peak around 1800 cm^{-1} are clearly visible while they are much smaller in case of the second exposure. It looks like that more hydrogen was adsorbed and more alanes were formed during the first contact of the surface with hydrogen. But this is not necessarily the case. As described above hydrogen exposures etch the surface. Thus the crystal was etched in the first part of the experiment and so its surface is rougher in the second one. The signal for the alanes might be screened.

Figure 5.11 shows a schematic picture for the etched surface. Some of the H atoms and alanes are located in gaps of the surface which has a high average refraction index n (including Al and vacuum). Given the selection rules (only components perpendicular to the surface are detectable), there is a strong screening of the H mode for hydrogen in the gaps. Only the H on top, were n = 1, are clearly visible, which results in a weaker signal. Another explanation could be that more of the alanes lie parallel to the surface when it is rougher and that explains why they can not be seen in IRRAS. It is also apparent that the broad band around 1700 cm^{-1} is more intense in case of the second exposure. This can be associated with the formation of larger alanes.

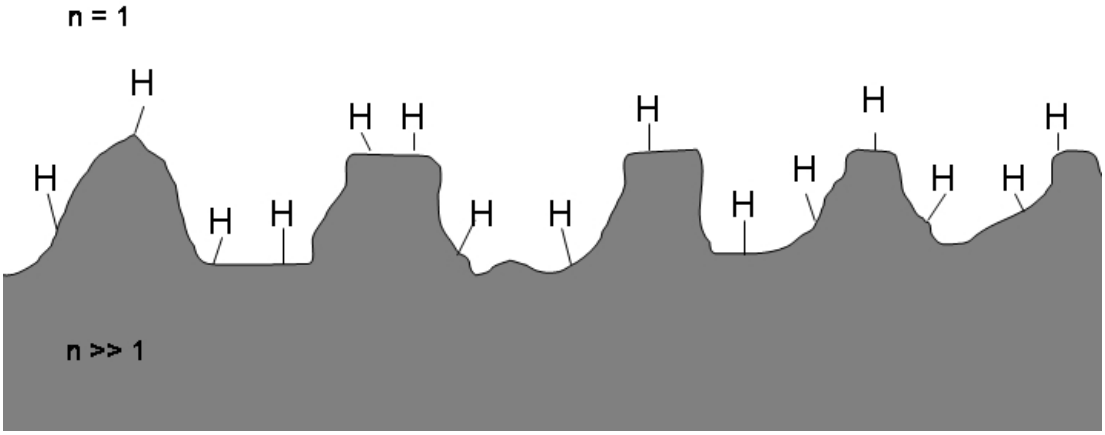

Figure 5.11: Schematically picture for H adsorbed to the etched surface. The signal of the atoms in the gaps is screened due to the high absolute value of n.

The same experiments were repeated with a higher H dose. The saturation H-coverage can be seen in the upper part of figure 5.10. Apparently the saturating coverage seems also higher for the first exposure. The possible explanation for this effect is the same as described above.

5.4 Conclusion

In agreement with the literature the formation of different sizes of alanes was observed when the Al(111) surface was exposed to atomic hydrogen. For low exposures vibrational bands of H atoms bound to Al terraces and step-edges were found together with features

corresponding to small alanes. With an increasing hydrogen dose the formation of larger aluminum hydrides is favored. As soon as saturation is reached the amount of H bound to the surface or to alanes stays constant.

It was also observed that the formation of alanes is temperature dependent. Higher sample temperatures result in the formation of larger alanes. This may be due to an increased mobility of small alanes which combine to larger alane clusters as soon as they hit each other. Moreover saturation is reached earlier in case of hotter surfaces.

Exposing the Al(111) surface to atomic hydrogen affects the surface roughness. Experiments with two exposures and one desorption of H and alanes in between leads to the formation of rougher surfaces. Less hydrogen absorption can be seen in case of the rougher surface maybe due to a screening effect.

Chapter 6

Titanium Doping of the Al(111) Surface

6.1 Introduction

An important step in the direction to do measurements of hydrogen interaction on Ti-Al surfaces is to dope our Al sample with titanium. A reliable and reproducible method of doping the surface of the Al(111)-sample must be found.

Theoretical calculations done at Brookhaven indicate that a Ti surface coverage of around 0.05 monolayers is most favorable for hydrogen dissociation. A monolayer (ML) is a single layer of atoms or molecules. The (111) surface of a fcc Al crystal has a closed backed surface with an atomic distance $a = 2.85\text{Å}$ [7]. The surface density ρ can be calculated by

$$\rho = \frac{1}{a^2 \sin 60^\circ}. \tag{6.1}$$

Thus one monolayer of a closed packed surface with the same atomic distance as Al has a density of $1.63{\cdot}10^{15}$ atoms/cm^2.

Figure 6.1 shows the typical mechanisms describing the growth of an overlayer on a substrate together with its characteristic variation of the Auger peak intensity. The first model, called Fran-van der Merwe, is based on a layer by layer growth. A new atomic layer starts as soon as the one before is finished. In the second mechanism (Stranski-Krastanov) the starting situation is the same. First an uniform atomic film of some monolayers grows on the surface. As soon as a critical layer thickness is reached the mechanism changes and the growth continues in form of three dimensional islands. If this formation of three dimensional crystallites starts right away from the substrate and bare spots on the surface remain the mechanism is called Volmer-Weber. Each of these models results in a different intensity evolution for the Auger peaks of the substrate and

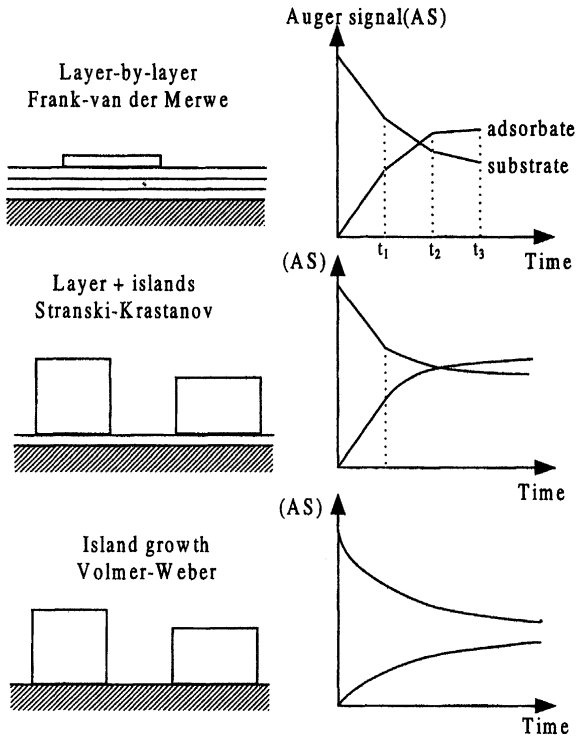

Figure 6.1: Different models describing the growth of an overlayer on a substrate together with its characteristic variation of the Auger peak intensity (taken from [2])

the adsorbate. In the layer-by-layer model a series of linear segments are visible. With each new atomic layer the gradient of its plot changes. The graph for the island growth shows a completely different behavior. The intensity associated with the adsorbate is increasing smoothly while the substrate is decaying in the same way. Since the Stranski-Krastanov mechanism is a intermediate form of the two other extremes its plot contains features of both other models. It starts with one or more linear segments and goes over to a smooth decay or increase as soon as the island formation begins [2].

The growth of thin Ti films on different aluminum surfaces has been studied. The behavior of Ti during deposition on polycrystalline aluminum has been investigated by C. Palacio and A. Arranz [24] [25]. They propose a Stranski-Krastanov growth mechanism where the first five atomic layers are formed out of a Al-Ti-alloy (Ti_2Al_3) followed by islands of pure titanium.

For single crystal substrates the formation of thin titanium films was found. On the Al(110) and Al(001) surfaces a pseudomorphic structure grows of fcc Ti for the first 5 to 5.5 monolayers. After that Ti islands begin to grow [26] [27] [28].

The formation of hexagonal closed packed Ti(0001) films on Al(111) was reported by R. J. Smith et al. [7] [28]. From their studies they conclude a Stranski-Krastanov growth mechanism consisting of two monolayers of a closed Ti film followed by a well ordered Ti island formation. After a deposition of 12 monolayers the islands coalesce and form a relatively smooth overlayer. The hcp Ti layer has lattice constants a = 2.95 Å and c = 4.68 Å which makes it incommensurate with the fcc Al crystal having an atomic distance of 2.86 Å . According to equation 6.1 the surface density of the hcp Ti surface is $1.33 \cdot 10^{15}$ atoms/cm^2.

6.2 Experimental Procedure

As described earlier we use a self built Ti-source to dope our Al sample with titanium. The source is installed in a manipulator and can be moved forward and backward. Thus it can be separated from the UHV-chamber by a valve. Moreover a shutter is mounted next to the valve which makes it possible to block the Ti beam even if the source is in use.

The Ti-source needs to be outgassed for at least a whole day to avoid unnecessary contamination of the sample. Therefore the current in the filament is slowly increased from 0 to around 4.2A. At a current of 2.5A the high voltage is switched on. With increasing current in the filament we can register an emission current at the high voltage power supply. As soon as the emission current reaches around 70 mA we are able to deposit Ti atoms at a low rate.

Before we can start the deposition we have to determine the exact deposition rate. For this purpose the Al sample is brought in a position so that it does not face the Ti-source. Next we move a quartz crystal monitor in front of the source. The monitor is water cooled to avoid changes of its signal due to the increasing temperature as soon as it is exposed to the source. Now the shutter is opened and the deposition on the

quartz crystal can be measured. The time for growing 1 Å is recorded. Usually we want to find the settings for a deposition rate of around 1 Å in 10 min. Unfortunately there is no way to tell how reliable the quartz crystal monitor shows the real thickness of the Ti-film. To make sure that we reach a thermal equilibrium this process is monitored for around one hour. As soon as this step is accomplished the shutter is closed, the monitor is removed and the sample is put in front of the source. For the actual deposition the shutter is opened for the desired time and then closed again. During a deposition of 5 min the temperature in the sample raises about 2°C. The pressure in the UHV-chamber varied between $7.7 \cdot 10^{-10}$ and $1.0 \cdot 10^{-9}$ Torr.

To determine the amount of Ti which was deposited Auger Electron Spectroscopy is used. Usually two spectra were taken. One without and one with an amplitude magnification of 20. Recording a spectrum without magnification makes it possible to quantify the Al peak at 68 eV while the higher amplification makes it possible to have a more detailed view on smaller peaks. The first set of experiments was performed with an analog x-y-scriber. For the later measurements an A/D-converter-PCI-card was available to display the result on the computer. As soon as the signal reaches an amplitude higher than ±10V it is cut off or produces artifacts.

Beside AES, Low Energy Electron Diffraction (LEED) measurements were performed. Therefore the Al sample was always brought in the same position in front of the LEED and the best settings for sharp LEED pattern were adjusted. We tried to keep these settings for the whole experiment. The patterns were recorded with a digital camera.

6.3 Results and Discussion

6.3.1 Low Ti-Depositions at T=105K

In this experiment the Al sample was cooled down with liquid nitrogen to a temperature of 105K. The deposition rate was around 1 Å in 11 min. We started with a deposition of 30 s after the reference AES and LEED measurements were completed. The second deposition was again 30 s followed by steps of 1 minutes up to a total of 4 min. According

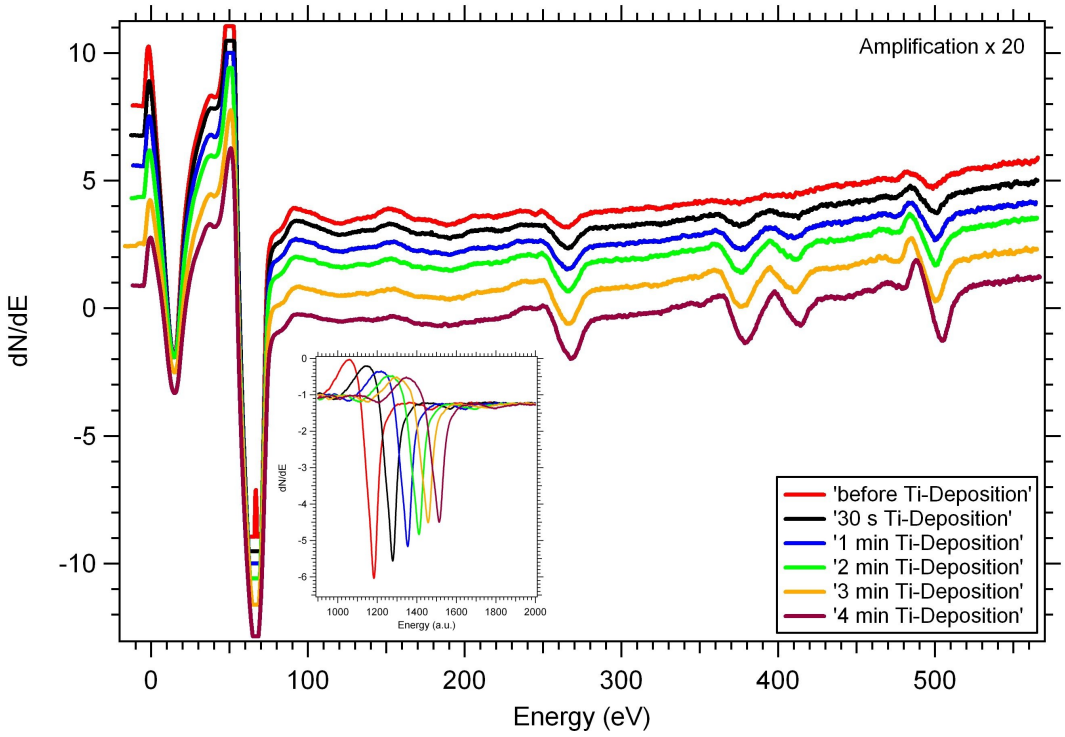

Figure 6.2: Set of AES spectra during Ti deposition at T=105K. The inset shows the evolution of the Al peak. To make the height differences more clearly the later peaks are shifted to the right.

to the quartz crystal monitor we should have deposited a total of amount of 0.36 Å which corresponds to 0.15 monolayers of Ti. Between every deposition two Auger spectra and two LEED pictures were recorded.

Figure 6.2 shows the AES with an amplification of 20. The Ti-double peak at 387 and 418 eV is clearly growing. This proves that our method of doping is working. Unfortunately the peaks of oxygen (at 503 eV) and carbon (at 272 eV) are also increasing, most likely due to the fact that the sample is cold and thus CO adsorbs dissociatively on Ti more easily than on a warmer surface.

The evolution of the Al-peak can be followed in the small inset in figure 6.2. In this inset Auger spectra were recorded without amplification. To make the comparison of the height easier, the peaks are shifted to the right as a function of deposition time. The height of the peak decreases with longer deposition time. This observation is connected to shrinking amount of Al atoms in the surface area which can be probed by Auger

electrons. Thus it confirms the formation of Ti and maybe also other elements on the surface.

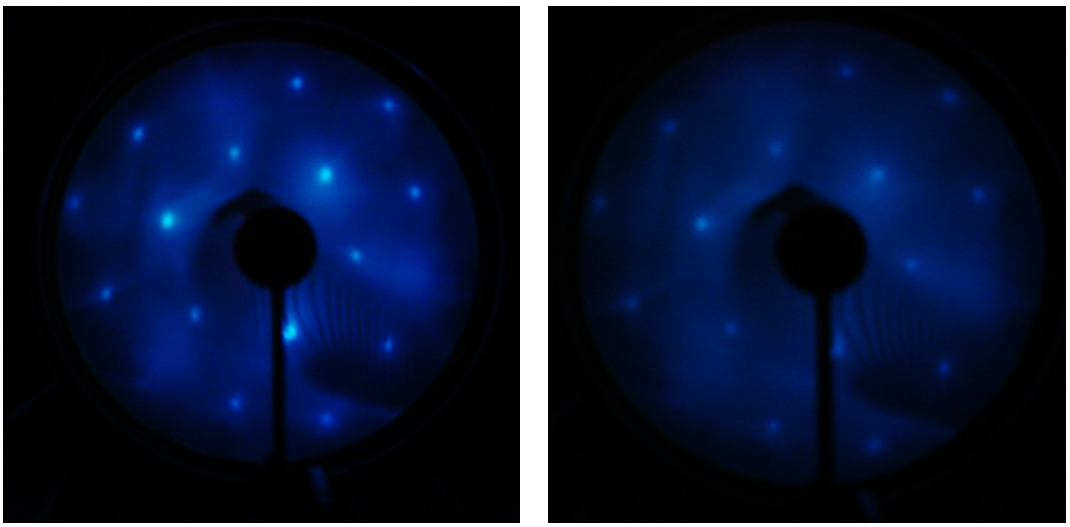

(a) Al(111) (b) after 4 min Ti-deposition

Figure 6.3: LEED patterns at an energy of 214.5 eV for low depositions at T=105K

Beside AES measurements also LEED patterns were photographed. A clean Al(111) surface is imaged in Fig. 6.3(a). Because the sample was cooled down to 105K it was possible to obtain a sharp LEED pattern even at a high energy of 214.5 eV. Figure 6.3(b) shows the same surface after 4 min of Ti-deposition. Apparently the same structure is visible but now it is a little less intense.

We conclude that we are able to deposit Ti on the Al surface. Using a cold sample has the disadvantage that a lot of contaminations stick to the surface. More investigations are needed to determine the amount of the deposition. The adsorbate layer could be completely removed by 6 Ar-sputtering cycles after the experiment. Thus the layer can not be very thick. To avoid the formation of an alloy, the sample was not annealed until the AES showed the absence of Ti.

6.3.2 Low Ti-Depositions at Room Temperature

A similar experiment was performed at room temperature. Again the deposition rate was around 1 Å in 11 min. A total deposition time of 2 min was reached in steps of 30 s. Thus the total surface coverage of Ti should be 0.18 Å , i.e. 0.077 monolayers, if

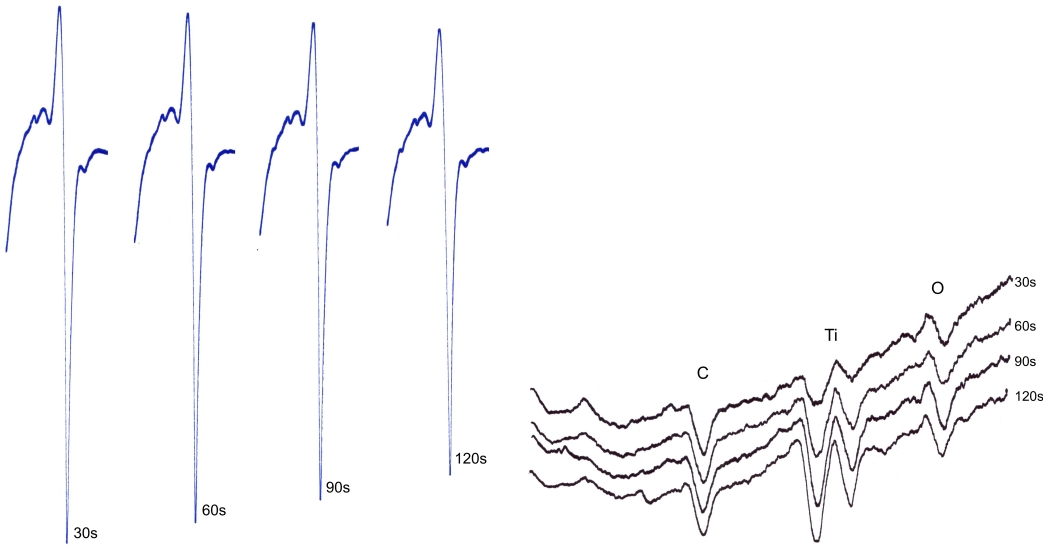

(a) Al-peak (b) Ti-peaks

Figure 6.4: Evolution of the Al peak 68 eV and the Ti-peaks at 387 and 418 eV for low exposures at T=290K. Apparently the height of the carbon (272 eV) and oxygen (503 eV) contamination stays almost the same.

the rate from the quartz crystal monitor is correct. Figure 6.5(a) shows the evolution of the Auger peak during the deposition at an amplification of 2. At the time these AES measurements were taken the analog x-y-scriber was still in use. The same trend as in the other low temperature experiments can be observed. Apparently the height of the Al-peak is decreasing with increasing deposition time.

The reverse situation could be found for the Ti-double peak. As seen in figure 6.4(b) it is clearly growing with higher Ti-deposition. Moreover this time the amount of oxygen and carbon contamination stays almost constant during the different depositions.

LEED pictures before and after the deposition were taken at an energy of 93.0 eV (figure 6.5). In both cases the characteristic hexagonal symmetry for an closed packed surface is visible. Again the fist image 6.5(a) is sharper than the last one (Fig. 6.5(b)).

6.3.3 Higher Ti-Depositions at Room Temperature

After the first experiences with doping small amounts of Ti on Al we increased the dose. The depositions were performed at around 26°C. This time the deposition rate measured by the quartz crystal monitor was 1 Å in 10 min. All exposures except the

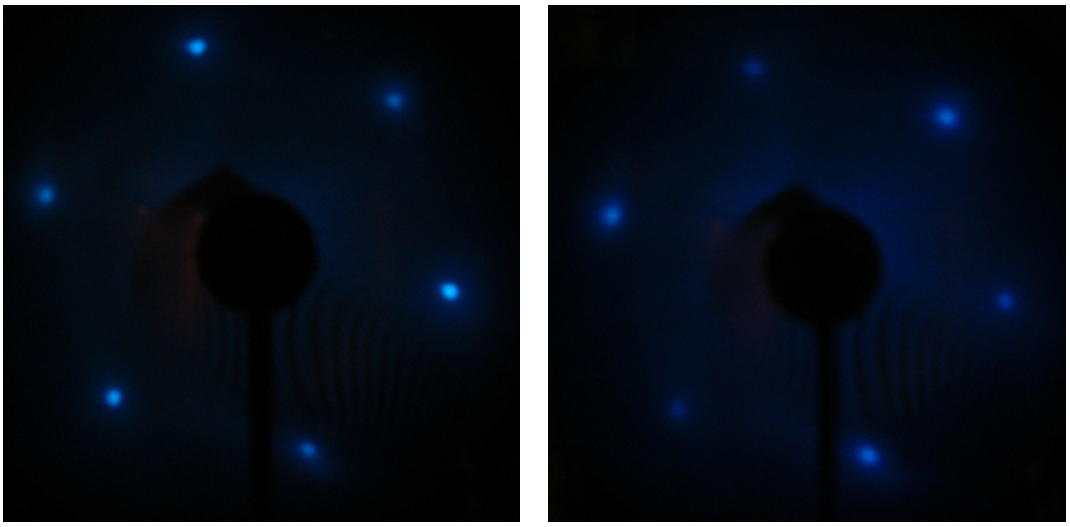

(a) Al(111) (b) after 2 min Ti-deposition

Figure 6.5: LEED patterns at an energy of 93.0 eV for low depositions at T=290K

second were for 5 min. The second one was only for 2 min. With a total deposition time of 23 min a Ti film of 2.3 Å was grown if the deposition rate shown by the monitor is correct. This would correspond to around 1 monolayer of Ti on the Al surface. Thus the amount is much higher than what was calculated to be the most favorable amount to dissociate molecular hydrogen. We deposited this relatively high adsorbate layer to check whether we can see reconstructions of the surface in LEED and to make our results more comparable to the existing literature. The goal is to properly calculate the thickness of the Ti coverage.

The results of the AES can be seen figure 6.6 for an amplification of 20. It is clearly visible that the Ti peaks at 387 and 418 eV are strongly growing. At the same time the Al peak loses intensity as shown in the inset for an amplification of 1. Again the peaks are manually shifted to the right in case of higher deposition times to make the evolution more clearly. The height of the Al peak decreases so drastically that even at the highest resolution of 20 it can be completely displayed on the screen in case of the last 3 Auger spectra. For lower Ti coverage the signal is cut off at an amplitude of ± 10V. After a deposition time of 23 min the height of the Ti-peak at 387 eV is approximately the same as the one of the Al peak. But this does not mean that the amount of Ti atoms in the first few monolayers is the same as for the Al. Different elements have different cross

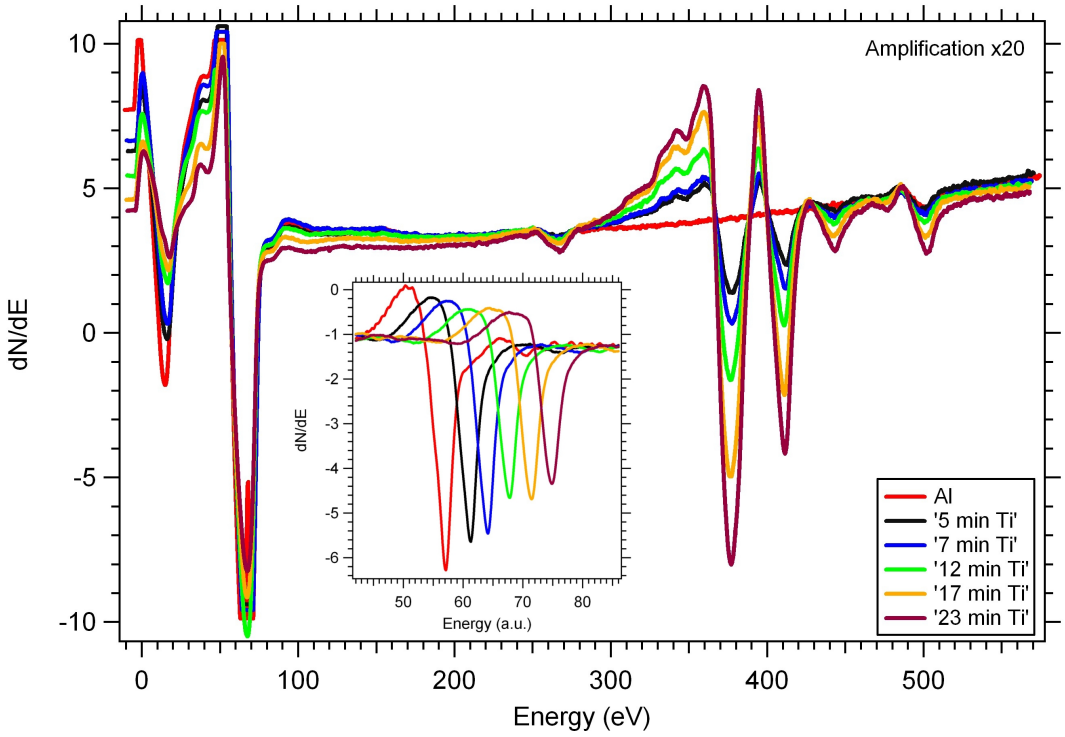

Figure 6.6: Set of AES spectra during Ti deposition at T=300K. The inset shows the evolution of the Al peak. To make the height differences more clearly the later peaks are shifted to the right.

sections in Auger Electron Spectroscopy. Because of the long times for deposition and the measurements the sample is contaminated with carbon and oxygen. Apparently the oxygen peak grows faster than the carbon peak.

For higher Ti deposition another titanium peak is appearing at 28 eV. This peak is only visible at an amplification of 1. Our Auger system does not display it at the highest amplification of 20. Figure 6.7(a) shows the evolution of this peak in comparison with the one of the aluminum at 68 eV. After the last deposition the ratio of Ti to Al is approximately 1 to 5. A similar graph for low energy AES measurements on Ti and Al can be found in the literature [24]. This work done by C. Palacio and A. Arranz can be seen in fig 6.7(b). The topmost spectrum shows a clean polycrystalline Al surface and the one on the bottom a pure titanium sample. In between they display the increasing of the Ti peak and the decreasing of the Al intensity during deposition of titanium. Moreover they find that the maximum of the Al feature is slightly shifted in that process. As mentioned earlier they claim that an alloy formation takes place

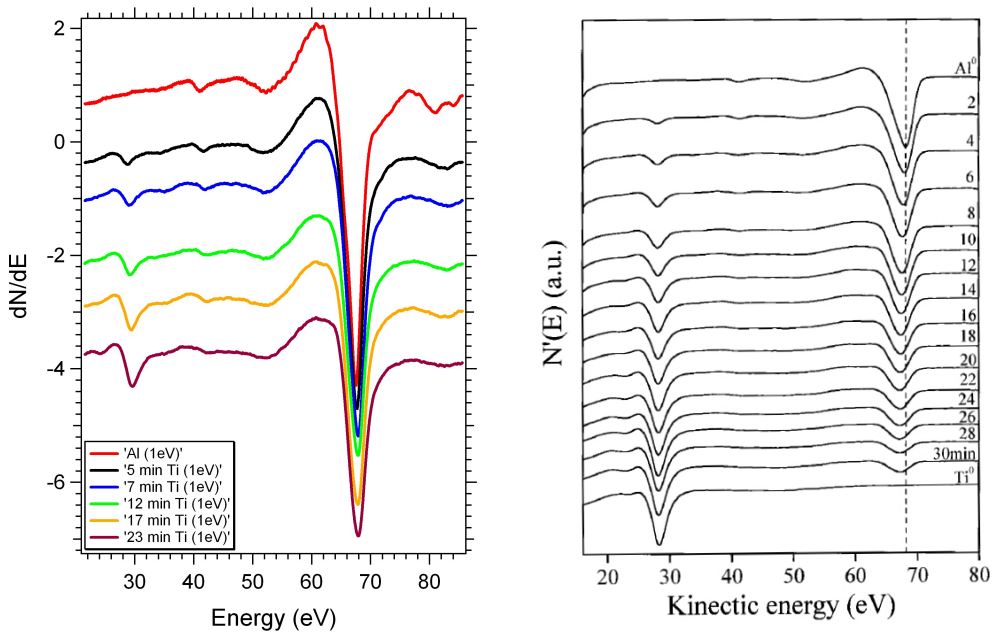

(a) our experiment (b) taken from [24]

Figure 6.7: Evolution of the low energy Ti peak in comparison with the Al peak.

for the first 4 monolayers (which corresponds to 10 min of deposition in their graph) followed by the growth of pure Ti islands. When we compare the peak heights in their measurements with ours we find that the 1 to 5 ratio which would be located somewhere between their spectra for 2 and 4 min. Thus, if their method is correct, we would have a film of approximately 1 monolayer of Ti_2Al_3 on our sample at the end of our experiment. This would result in an amount of titanium which is enough to form 0.4 monolayers of the pure element. But it is hard to determine how good these two experiments can be compared. First of all they work with polycrystalline Al which might form a different structure. Moreover we do not know the amount of other surface contaminations on their sample which also influences the height of the Al peak.

A way to obtain information about the thickness of the Ti film is to calculate the Ti concentration in the sample using the heights of the Auger peaks. Since we did not measure an Auger reference spectrum of a pure Ti crystal with our system we can not present accurate calculations. Moreover we do not know whether the Ti atoms form a layer on top of the Al, whether this layer is complete or if the titanium atoms diffuse

in the first few monolayers of the bulk. What we can present are estimations which use some rough approximations.

One possibility is to assume that the Ti is uniformly distributed in the first two monolayers of the surface and that only the first two ML contribute to the Auger signal. The second approximation is reasonable because electrons of the low energy corresponding to the LMM Auger peak for aluminum (68 eV) have an inelastic mean free path of only around 3.5 Å in Al [29]. The inelastic mean free path λ(E) is the distance an electron beam of the energy E can travel through a material before its initial intensity decays to 1/e [2]. The relative concentration of two elements can be calculated [2] using

$$\frac{c_{Ti}}{c_{Al}} = \frac{I_{Ti}}{I_{Al}} \frac{\sigma_{Al}}{\sigma_{Ti}}. \tag{6.2}$$

Here I is the peak to peak height and σ is the relative sensitivity factor of the corresponding MLL auger peak (at 68 eV for Al and at 418 eV for Ti). The heights were measured in the spectrum which was taken after 23 min of deposition at an amplification of 20. For aluminum we find I_{Al}=4.86 and for Ti we find I_{Ti}=2.11. Using tabulated values [30] for the relative sensitivity factor gives us σ_{Al}=0.025 and σ_{Ti}=0.440. Thus we calculate the ratio to

$$\frac{c_{Ti}}{c_{Al}} = 0.36. \tag{6.3}$$

If the assumption made above is correct the amount of Ti would correspond to around 0.72 ML of pure Ti.

Another possible assumption is that the Ti stays on top of the Al crystal and forms one complete atomic layer. The attenuation of the aluminum Auger signal through this Ti adsorbate can be described [2] by

$$I_{Al} = I_{Al}^0 e^{-d_{Ti}/\lambda_{Al}}, \tag{6.4}$$

were I_{Al} is the intensity after and I_{Al}^0 the intensity before the deposition. We are interested in the thickness d_{Ti} of the Ti film which can be calculated by

$$d_{Ti} = -\lambda_{Al} \ln \frac{I_{Al}}{I_{Al}^0}. \tag{6.5}$$

To get the values for the peak to peak heights (I_{Al}=4.86 and I^0_{Al}=6.36) the spectra without amplification before and after 23 min of Ti deposition were used. We find a thickness of

$$d_{Ti} = 0.94 \text{ Å}, \tag{6.6}$$

which would correspond to around 0.4 ML of Ti.

Figure 6.8 shows the LEED pattern before (6.8(a)) and after (6.8(b)) a deposition of 23 min. These pictures were recorded at an energy of 53.5 eV. In the fist picture the typical hexagonal shape can be seen. The same structure is visible in the second LEED pattern but the spots are less intense. Similar observations can be found in the literature [7]. Kim et al. observed a fading out of the LEED pattern, which were clear in the beginning (Fig. 6.8(c)), for deposition smaller then 2 monolayers (ML). They performed their experiments with a similar energy of 52.8 eV. For higher depositions up to 10.4 monolayers they see the hexagonal symmetry again but now with broad beam spots (Fig. 6.8(d)). They associate this behavior with the formation of well ordered Ti islands. We could not observe these broader features. This is consistent with the amount of Ti we expect in our experiment.

After the experiment the titanium had to be removed form the surface by argon sputtering. To avoid the formation of an alloy, the sample was not annealed before the AES measurements confirmed that no Ti is left on the surface. The decrease of the Ti double peak can be observed in figure 6.9. The curve on the bottom shows the peak height at the end of the deposition. After 6 sputter cycles at 1.5 keV most of the Ti is already removed. Thus the deposited film was not very big. In the curve after 16 cycles only a very small amount of Ti is left. This could be either Ti that diffused deep in the bulk or it is simply a contamination of the Auger electron gun which happened during the deposition.

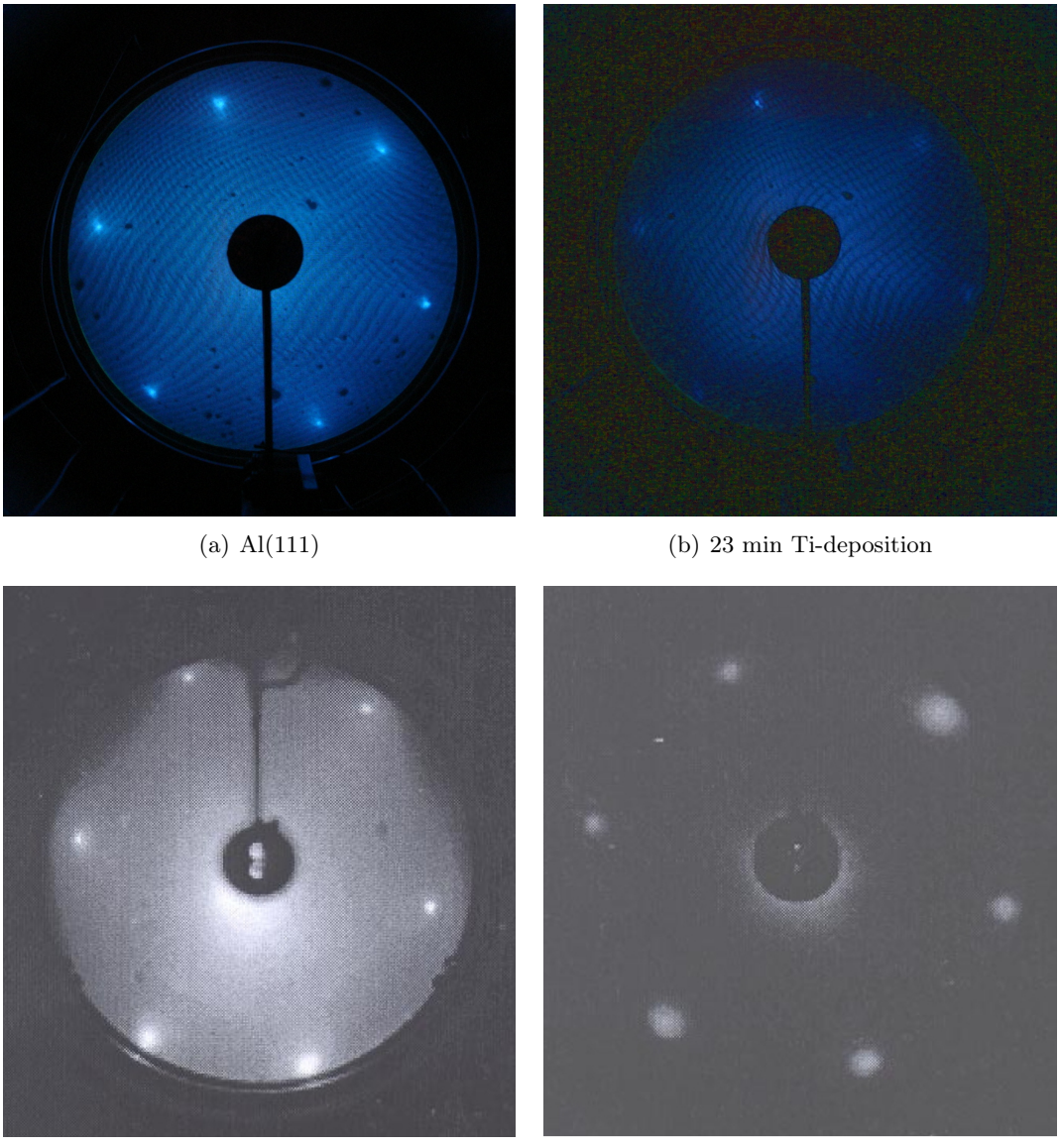

(a) Al(111)

(b) 23 min Ti-deposition

(c) Al(111) taken from [7]

(d) 10.4 ML Ti-deposition taken from [7]

Figure 6.8: LEED patterns which were observed in our experiment at an energy of 53.5 eV in comparison with LEED pictures from the literature [7] recorded at 52.8 eV.

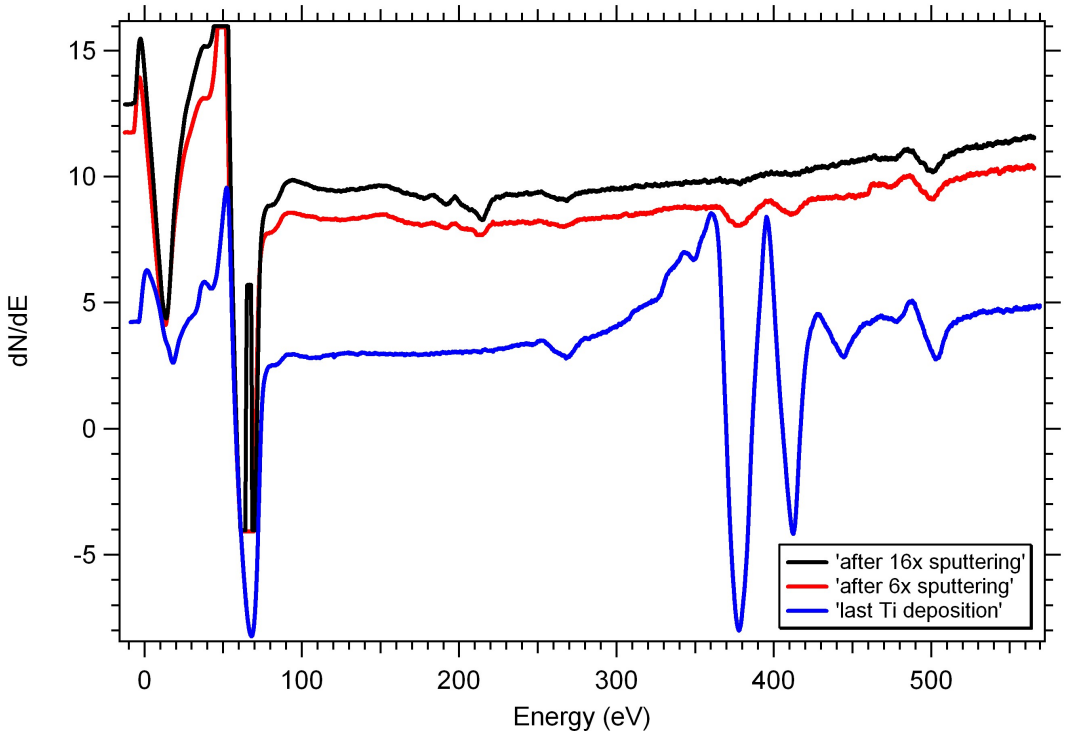

Figure 6.9: Set of AES spectra showing the decreasing of the Ti double peak due to sputter-cleaning of the surface. Apparently most of the Ti overlayer could be already removed with 6 sputtering cycles.

6.4 Conclusion

We are able to deposit Ti in a reliable and reproducible way on our Al(111) substrate. Besides measuring the deposition rate before the experiment with a quartz crystal monitor AES is the best method to determine the amount of Ti on the surface. No reconstruction of the surface could be observed in LEED. At this stage of the experiment the absolute Ti coverage can not be determined precisely. A possible way to calibrate the thickness of the Ti-film would be to use Rutherford Backscattering Spectroscopy (RBS) and to correlate the Auger measurements with these results. To do this a small silicon sample should be placed in the UHV chamber and the Ti deposition should be performed under the same conditions as for Al. Then the Si sample should be removed and the RBS measurements have to be performed. We can not use our Al(111) sample because as soon as we remove it from the chamber an oxide layer would form which alters the surface. Moreover the sample could be heavily contaminated during RBS.

Depositing the Ti at room temperature minimizes contaminations of the surface compared to depositions at low temperatures. This can be explained by less adsorption of dirt on the sample. The question whether we form a pure Ti- or an alloy-overlayer remains unanswered.

Chapter 7

Infrared Study of Solid State Aluminum-Hydride

7.1 Introduction

In this part of the work solid state aluminum trihydride (AlH_3) was investigated with IR-spectroscopy under high vacuum conditions. These experiments were performed to check whether there exist similarities between the solid state AlH_3 and the AlH_3 formed when aluminum is exposed to atomic hydrogen.

AlH_3 is a covalent binary hydride which exists in at least seven different polymorphs, namely $\alpha, \alpha', \beta, \delta, \epsilon, \gamma$ and ζ [31]. Of all these polymorphs the α version is reported the most stable one [32].

It desorbs in the reaction

$$AlH_3 \rightarrow Al + \frac{3}{2}H_2 \tag{7.1}$$

to hydrogen and Al powder. The temperature range where the reaction takes place is between 175 and 200°C. The theoretical amount of hydrogen gained by this process is 10.1 wt%. Since this reaction is highly favorable for thermodynamic reasons it is hard to reverse the process. For rehydriding a H_2 gas pressure of 2.5 GPa is required. Despite of being metastable at room temperature AlH_3 usually does not decompose because it is coated by an Al_2O_3 passivation layer [33].

Our sample material is an α (trigonal/rhombohedral) version of AlH_3 which was produced in 1975 by Dow Chemical. It consists of translucent cuboidal particles having a size of 50-100μm. Since the material is old it contains only around 8 wt% [33] H compared to the theoretical value of 10.1 wt% for pure AlH_3 [33].

7.2 Experimental Procedure

4 to 35 mg of the AlH_3 powder were mixed with 200 mg KBr powder and pressed to circular pellets with a diameter of 1.3 cm (see Fig. 7.1 b). Since the KBr is transparent for IR-radiation it is the ideal material for creating the pellets. Moreover pellets with 25 to 75 mg of pure AlH_3 were produced. These pellets are not very stable and most of the times it was not possible to obtain a circular disc (see Fig. 7.1 d). They tend to fall apart if they were not handled carefully enough when they were put or removed from the sample holder. Pellets out of pure AlH_3 with more than 70 mg were not transparent enough for IR transmissions measurements.

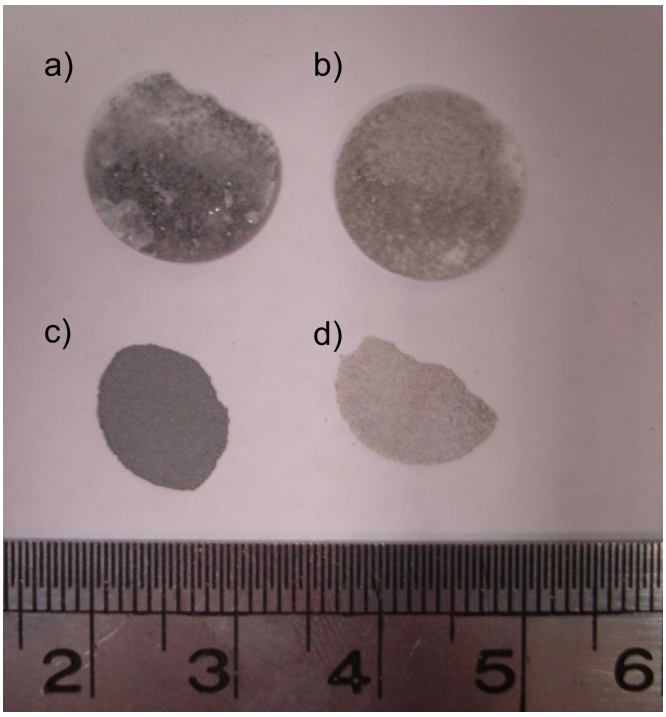

Figure 7.1: Different AlH_3 samples: Mixture of AlH_3 and KBr after (a) and before (b) annealing to 250°C; Pellets out of pure AlH_3 after (c) and before (d) annealing to 250°C

The pellets were mounted on a sample holder and placed in a small chamber, which can be pumped down by a turbopump to a pressure of $5.0 \cdot 10^{-7}$ Torr. The chamber is a commercial available High Pressure High Temperature Cell produced by Specac Limited under the product number P/N 5850. Thus the cell can be baked up to a temperature of 200°C and the sample holder even to 800°C. To make the cooling down process faster

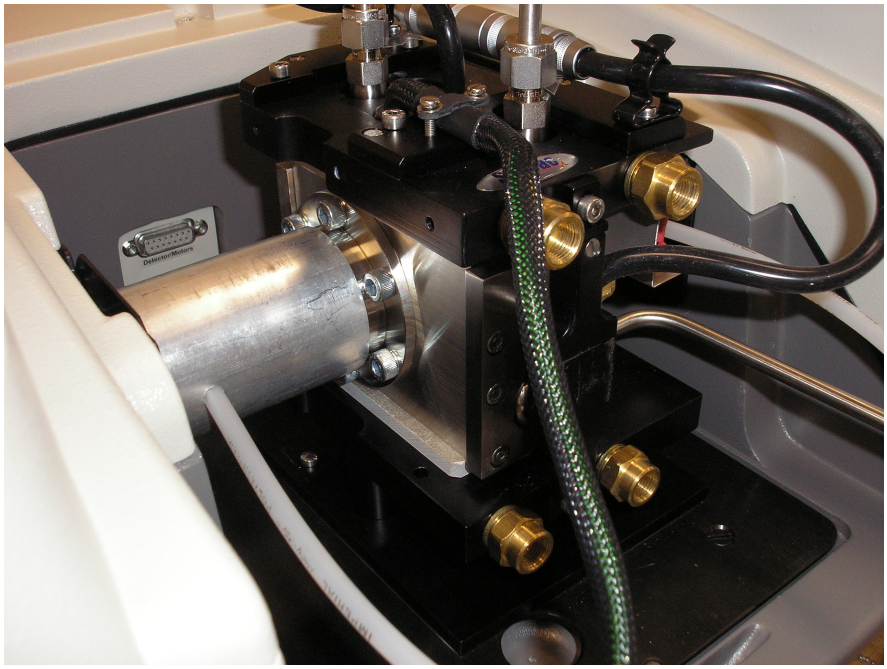

Figure 7.2: The cell in the Thermo Nicolet Nexus 670 spectrometer which was used for investigating the solid state AlH_3.

and to hold a stable temperature the small chamber is also water cooled. Figure 7.2 shows a picture of the cell in the spectrometer. For recording the spectra a Thermo Nicolet Nexus 670 spectrometer with a MCT/A detector was used. All the data were acquired in a transmission mode.

7.3 Results and Discussion

7.3.1 Alanes Mixed with KBr

For this experiment a pellet consisting of around 25.8 mg AlH_3 powder mixed with 200 mg KBr was used. The sample was mounted in the sample holder and the chamber was pumped down to $1.6 \cdot 10^{-6}$ Torr. Moreover it was baked to a temperature of 110°C to get rid of water contaminations. Then the cell was cooled down to 28°C and spectra were recorded. As reference a spectrum of the empty baked and pumped cell was taken after the experiment. The absorbance was calculated following equation 3.14 and the baseline was corrected.

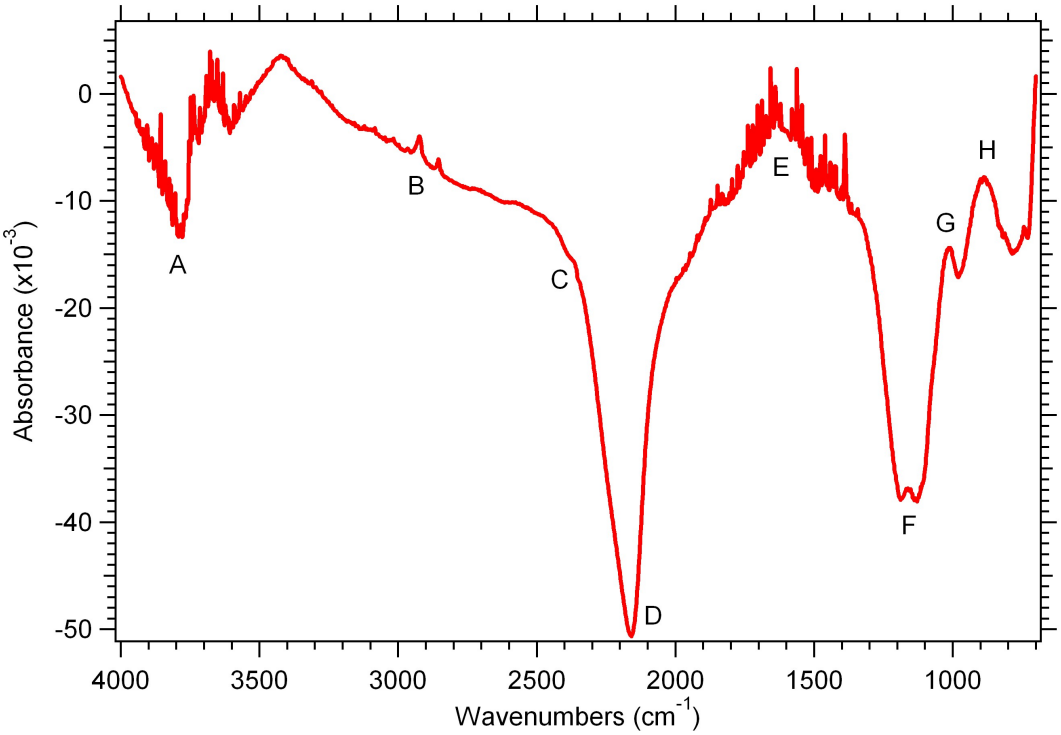

Figure 7.3: Spectrum of a solid state AlH_3 sample recorded in a pumped and baked cell.

Figure 7.3 shows the results. High absorbance can be observed for the wavenumber region 4000 to 2200 cm^{-1} and 2000 to 1300 cm^{-1}. Apparently there are two features of much smaller absorbance, one with a minimum at 2150 cm^{-1} (D) and one with two local minima at 1182 and 1122 cm^{-1} (F). Feature F shows a small peak in the middle of the minimum. These features might be associated either with the solid state alanes, their coating or with the KBr powder.

The small spiky features between 4000 and 3600 cm^{-1} (A) and 2000 and 1400 cm^{-1} (E) are vibrational modes of water in the purge of the spectrometer. The double peak B at 2917 and 2850 cm^{-1} and the peak at 1006 cm^{-1} (G) might corresponds to hydrocarbons. There is also a hardly visible band (C) at 2370 cm^{-1}. It is hard to tell whether the feature H is real or appears only because of a wrong baseline correction.

In the next step the sample holder was annealed to a temperature of 350°C and then cooled down again. As already mentioned earlier the AlH_3 should decompose to Al powder at a temperature higher than 175°C. Since our AlH_3 is in a pellet of KBr, which is not a good thermal conductor, we went to higher temperatures to make sure

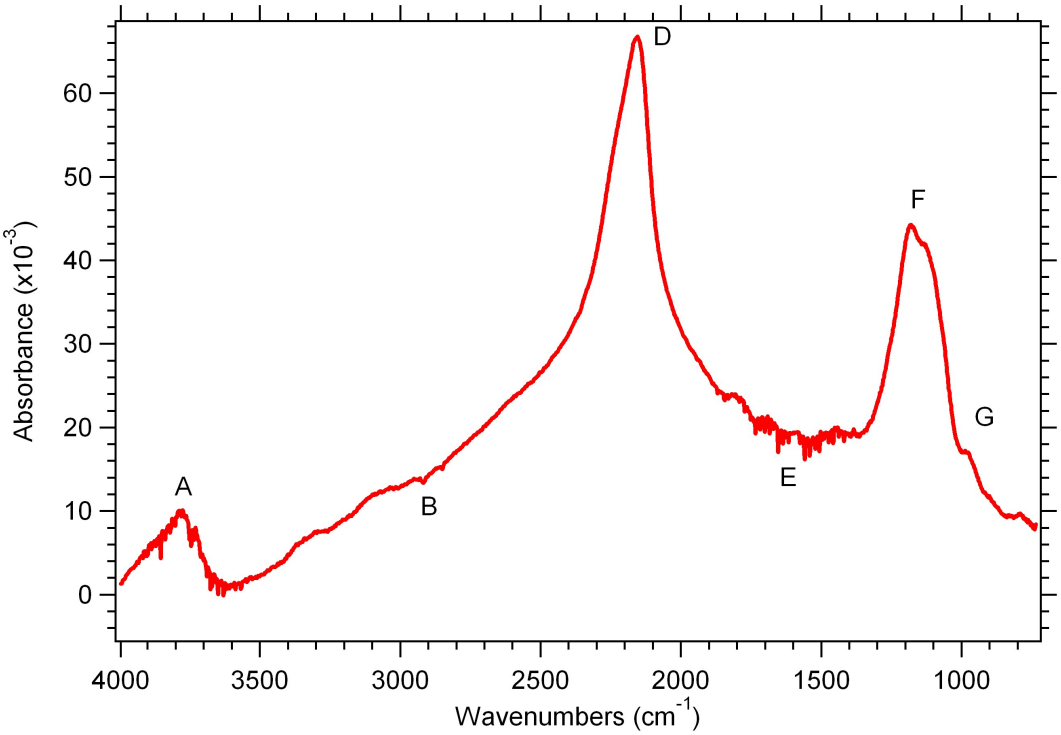

Figure 7.4: Difference of the absorbance after the solid state AlH_3 sample was annealed to 350°C.

that we see the decomposition. The absorbance calculated between the annealed sample and the sample before can be seen in figure 7.4. It is clearly visible that the structure *D* and *F*, which might be alanes, their coating or changes in the KBr, show a much higher absorbance after annealing.

As seen in figure 7.1 the sample changes its color when it was annealed. Thus the decomposition did take place and we should have Al powder as an educt in the sample. The AlH_3 has a lighter gray than the pure Al.

7.3.2 Evolution with Temperature

To take a closer look at the decomposition of AlH_3 with increasing temperature the following experiment was performed: 26.4 mg of AlH_3 powder was mixed with 200 mg KBr and pressed to a pellet. The sample was put in the cell, pumped down to $1.7 \cdot 10^{-6}$ Torr and baked for 1h at 115°C. Then a spectrum was taken at this temperature. After that the temperature was raised to 170°C and hold there for 7 min to make sure that

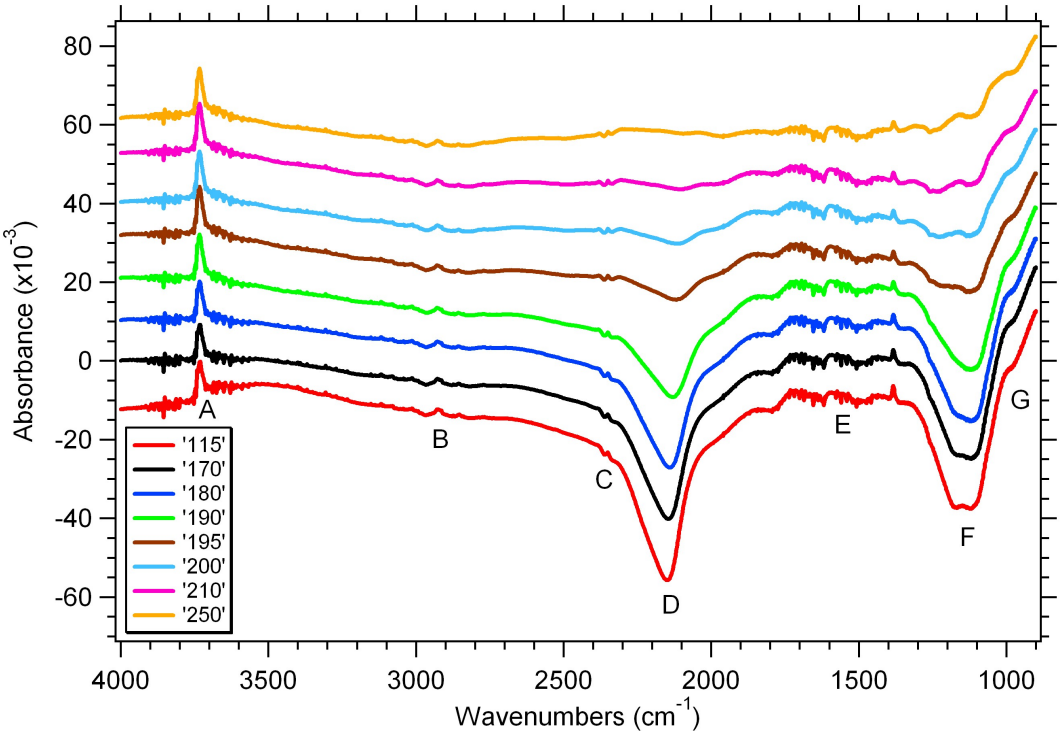

Figure 7.5: Absorbance of the solid state AlH_3/KBr sample as function of temperature (from 115°C to 250°C).

an equilibrium was reached before a spectrum was recorded. This step was repeated for different temperatures from 180 to 250°C. As soon as these measurements were finished the sample was removed from the cell and the empty cell was pumped and baked to obtain a reference.

Figure 7.5 shows the results for different temperatures. The situation at a temperature of 115°C is the same as described above. The feature D and F disappear starting at 170°C. At a temperature of 250 °C the feature D is completely gone while small rests of feature F remain. No changes can be observed for the peaks A, B, C, E and G. It is hard to make a reliable statement about the shape of the spectrum for wavenumbers below 1000 cm^{-1}.

7.3.3 Pure Alanes

In this part of the work the annealing experiment was repeated but this time with a pellet out of 35 mg of pure AlH_3. The sample was mounted in the chamber, pumped down to

$1.6{\cdot}10^{-6}$ Torr and baked to 115°C. As soon as it was cooled down to room temperature a spectrum was taken. After that the sample was annealed to 250°C, cooled down again and another spectrum was taken. The absorbance between the annealed and the not annealed sample was calculated according to equation 3.14 and is shown in figure 7.6.

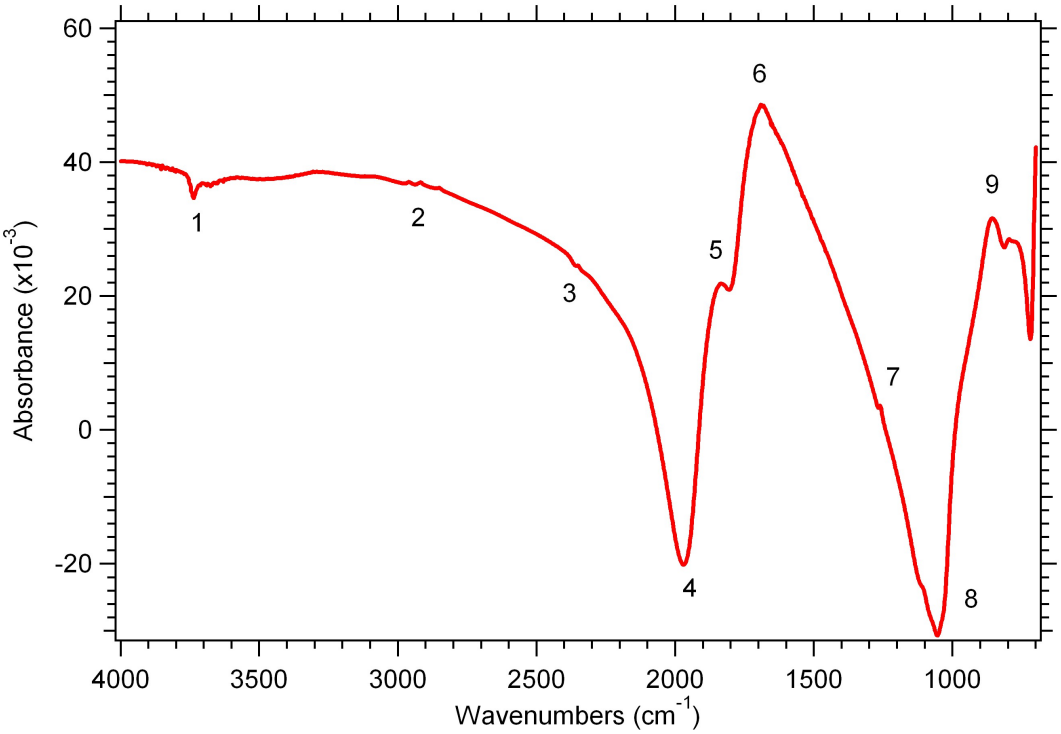

Figure 7.6: Absorbance of a pure solid state AlH_3 sample after annealing to 250°C.

The features 1, 2 and 3 are at the same wavenumbers than the features *A*, *B* and *C* in figure 7.3, 7.4 and 7.5. Two big minima in the absorbance are visible at 1970 cm^{-1} (feature 4) and 1055 cm^{-1} (feature 8). We associate these features with AlH_3 or its coating. The big peak 6 has its maximum at 1687 cm^{-1} and is accompanied by two smaller peaks one at 1836 cm^{-1} (feature 5) and one at 1261 cm^{-1} (feature 7). Another peak (9) can be found at 854 cm^{-1}. Again the sample changed its color when it was annealed (see figure 7.1) which is a indication the AlH_3 did decompose.

7.3.4 Comparison Between Pure Alanes and Alanes Mixed with KBr

Since the main features for the measurements with and without KBr are different, another experiment was performed. This time a smaller amount of KBr (55 mg) was

mixed 25 mg of AlH_3. The measurements were done in the same way as for the two other experiments and the sample was annealed to 230°C. The results for the absorbance are plotted in figure 7.7 together with the data obtained for a pure AlH_3 and AlH_3 mixed with 200 mg of KBr.

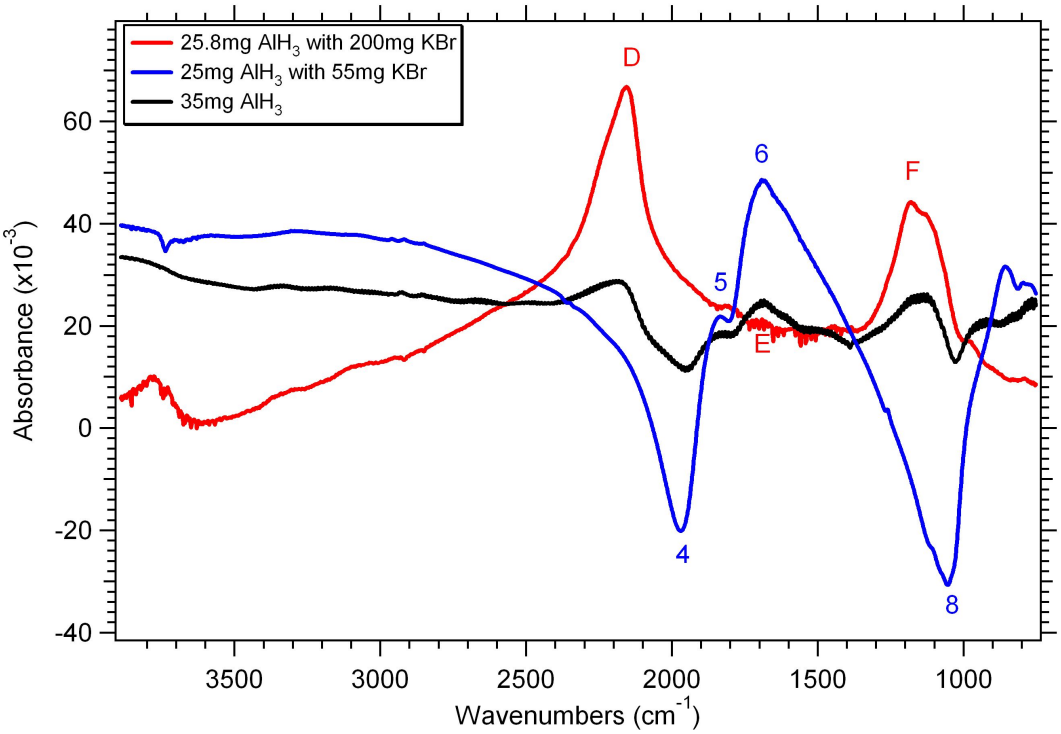

Figure 7.7: Absorbance between the not annealed and the annealed sample for pure solid state AlH_3 and alanes mixed with different amounts of KBr.

It can be seen that the absorbance for this experiment contains features of both other measurements. It looks like a superposition of the other absorbances. The first peak around 2175 cm^{-1} is similar to feature D while the following minimum can be associated with feature 4. A peak at 1835 cm^{-1} labeled 5 is visible in all the spectra. The next two peaks are nearly at the same position as feature 6 and F. Rests of a region with less absorbance are visible which correspond to feature 8.

Thus mixing AlH_3 with KBr influences the spectra and even the amount of the KBr is important. The observation could be accounted for by a strong dispersion of the pure AlH_3, leading to a "fano lineshape" with a strong negative component on the high frequency side of the absorption band. This hypothesis needs to be tested.

7.3.5 Comparison Between Solid State Alanes and Alanes on Al(111)

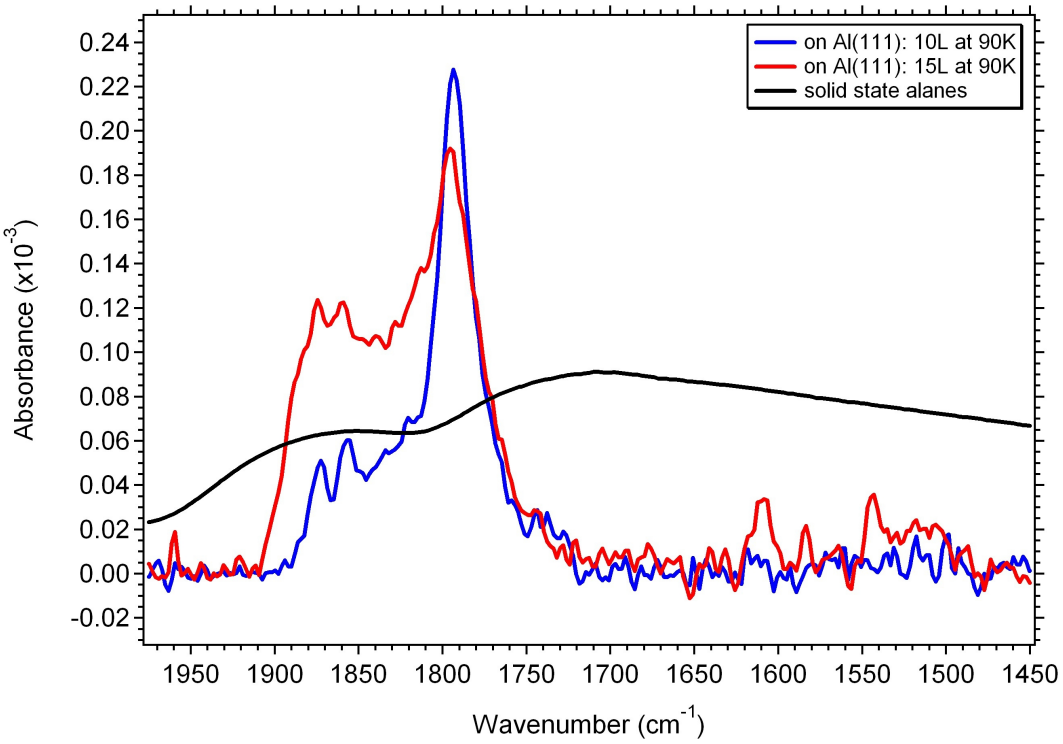

Figure 7.8: Comparison of the vibrational bands between solid state Alanes and Alanes on Al(111).

Figure 7.8 shows a comparison between alane formation on the Al(111) surface due to a low hydrogen exposure and the absorbance of solid state AlH_3 in the same wavenumber region. Apparently no similarities between the spectra can be found.

7.4 Conclusion

Features, which might be associated with the alanes or their coating, were found in the regions of 2100 to 1700 cm^{-1} and 1300 to 700 cm^{-1}. These structures do not fit to vibrational bands which were observed by Wong et. al. [34]. After the sample was annealed to 250°C the features change, which hints to the decomposition of AlH_3 to Al. Moreover this change is also visible when the color of the sample before and after annealing is compared.

It was found that mixing the alanes with KBr strongly influences the shape of the spectrum. At this stage of the experiment we have no final explanation for this behavior and closer investigations are necessary.

None of the observed vibrational bands of the solid state AlH_3 matches with the bands which were found in the case of alanes forming on the Al(111) surface.

Chapter 8

Summary

The interaction of atomic hydrogen with an Al(111) surface has been investigated using Infrared Reflection Absorption Spectroscopy (IRRAS). The experiments were performed under Ultra High Vacuum (UHV) at temperatures of 93, 180 and 259K. Beside H atoms binding to terraces and atomic steps the formation of different sizes of alanes (aluminum hydrides) has been observed. Different hydrogen coverages result in the growth of different alane clusters. For low exposures stretching bands of H-atoms and small alanes dominate. With increasing hydrogen exposure alanes of larger sizes grow. This can be seen by the evolution of a broad feature connected to the bridging frequencies of these alanes. Moreover the formation of the aluminum hydrides is temperature dependent. The growth of larger alanes is favored at higher temperatures. It was also observed that surface roughness influences alane formation. Surfaces which were exposed to hydrogen the first time seem to adsorb more H then surfaces which were exposed for a second time. This might be the effect of screening. Surfaces for the second exposure were rougher because they were etched by the first exposure and so alanes or H atoms located in gaps of the surface are probably not so intense in IRRAS.

In another step of the experiment the Al surface was doped with titanium atoms. For this purpose a Ti-source was designed and built. We determined the deposition rate with a water cooled quartz crystal monitor before the exposures. Sets of low exposures with a thickness of less then one monolayer were grown at 105K and at room temperature. Moreover we grew a Ti film of approximately 1 ML at room temperature and compared our results with the existing literature. The amount of Ti on the surface could be determined by Auger Electron Spectroscopy (AES). Thus evolution of Ti-peaks at 28, 387 and 418 eV can be displayed together with the decrease of the Al

peak for different depositions. Furthermore Low Energy Electron Diffraction (LEED) pattern were photographed before and after different Ti-depositions. The pictures show a typical hexagonal symmetry corresponding to a closed packed surface. With higher Ti deposition the spots loose intensity.

Solid state AlH_3 was studied with the powerful tool of Fourier Transform Infrared Spectroscopy (FTIR). Therefore a different experimental setup consisting of a cell which can be pumped down to a high vacuum in a conventional Nicolet FTIR spectrometer was used. These measurements were conducted using the transmission mode. Two features, which might be associated with solid state alanes, were observed at regions of 2100 to 1700 cm^{-1} and 1300 to 700 cm^{-1}. When the sample was annealed to 250°C the features changed which should be due to the decomposition of AlH_3 to Al and hydrogen. During the annealing process the sample changes its color. Moreover it was found that mixing the AlH_3 with KBr alters the spectrum significantly. All the observed features show no similarity to the vibrational frequencies of the alanes which form on Al(111).

References

[1] L. Schlapbach and A. Zuttel. Hydrogen-storage materials for mobile applications. *Nature*, 414(6861):353–8, 2001.

[2] G. Attard and C. Barnes. *Surfaces*. Oxford University Press New York, 1998.

[3] Stanford Research Systems. *Models RGA100, RGA200, and RGA300 Residual Gas Analyzer Operation Manual and Programming References*.

[4] `http://en.wikipedia.org/wiki/Image:Cut_through_turbomolecular_pump.jpg`, 2005.

[5] R Arnold. `http://www.ir-spektroskopie.de`, 2007.

[6] EP Go, K. Thuermer, and JE Reutt-Robey. H adsorption and the formation of alane oligomers on Al (111). *Surface Science*, 437(3):377–385, 1999.

[7] YW Kim, G. White, N. R. Shivaparan, M. A. Teter, and R. J. Smith. Growth and structure of hcp Ti films on Al (111) surfaces. *Surface Review and Letters(Singapore)*, 6(5):775–780, 1999.

[8] S. Satyapal et al. The U.S. Department of Energy's National Hydrogen Storage Project: Progress towards meeting hydrogen-powered vehicle requirements. *Catalysis Today*, 120(3-4):246–256, 2007.

[9] DK Ross. Hydrogen storage: The major technological barrier to the development of hydrogen fuel cell cars. *Vacuum*, 80(10):1084–1089, 2006.

[10] B. Bogdanovic and M. Schwickardi. Titanium-doped alkali metal aluminium hydrides as potential novel reversible hydrogen storage materials. *Journal of Alloys and Compounds*, 253:1–9, 1996.

[11] G. Sandrock, K. Gross, and G. Thomas. Effect of Ti-catalyst content on the reversible hydrogen storage properties of the sodium alanates. *Journal of Alloys and Compounds*, 339(1):299–308, 2002.

[12] F.O.H. John. *A user's guide to vacuum technology*. Wiley, 1980.

[13] Perkin-Elmer. *Instruction Manual PHI Model 04-131*.

[14] Leybold-Heraeus. *Operating Instructions TURBOVAC 150, 350*.

[15] Pfeiffer/Balzer. *Operating Instructions for Turbo-Molecular Pumps TPH 270, TPU 270*.

[16] M.D. Bertolucci and D.C. Harris. *Symmetry and Spectroscopy: An Introduction to Vibrational and Electronic Spectroscopy*. Oxford University Press, 1978.

[17] H. Haken and H.C. Wolf. *Molekülphysik und Quantenchemie: Einführung in die Experimentellen und Theoretischen Grundlagen*. Springer, 2002.

[18] R.J. Bell. *Introduction Fourier Transform Spectroscopy*. Academic Press, 1972.

[19] S.P. Davis, M.C. Abrams, and J.W. Brault. *Fourier Transform Spectrometry*. Academic Press, 2001.

[20] J. Paul. Hydrogen adsorption on Al (100). *Physical Review B*, 37(11):6164–6174, 1988.

[21] A. Winkler, C. Resch, and KD Rendulic. Aluminum hydride desorption from hydrogen covered aluminum single crystal surfaces. *The Journal of Chemical Physics*, 95:7682, 1991.

[22] Woodruff and Delchar. *Modern Techniques of Surface Science*. Cambridge University Press, 1994.

[23] S Chaudhuri. To be published, 2007.

[24] C. Palacio and A. Arranz. Spectroscopic characterization of the surface nanostructure of Ti during deposition on polycrystalline aluminium. *Surface and Interface Analysis*, 27(9):871–879, 1999.

[25] A. Arranz and C. Palacio. Ultrathin AlO_x-TiO_y film formation by controlled oxidation of titanium deposited on polycrystalline aluminum surfaces. *Journal of physical chemistry. B, Condensed matter, materials, surfaces, interfaces, & biophysical chemistry*, 106(37):9590–9596, 2002.

[26] A.A. Saleh, V. Shutthanandan, and RJ Smith. Observation of ultrathin metastable fcc Ti films on Al (110) surfaces. *Physical Review B*, 49(7):4908–4914, 1994.

[27] A.A. Saleh, V. Shutthanandan, NR Shivaparan, RJ Smith, TT Tran, and SA Chambers. Epitaxial growth of fcc Ti films on Al (001) surfaces. *Physical Review B*, 56(15):9841–9847, 1997.

[28] RJ Smith, YW Kim, NR Shivaparan, and G. White. Growth of thin Ti films on Al single-crystal surfaces at room temperature. *Surface and Interface Analysis(UK)*, 27(4):185–193, 1999.

[29] S. Tanuma, CJ Powell, and DR Penn. Material dependence of electron inelastic mean free paths at low energies. *Journal of Vacuum Science & Technology A: Vacuum, Surfaces, and Films*, 8:2213, 1990.

[30] L.E. Davis et. al. *Handbook of Auger Electron Spectroscopy*. Physical Electronics Division, 1978.

[31] J. Graetz and J.J. Reilly. Decomposition Kinetics of the AlH 3 Polymorphs. *Journal of physical chemistry. B, Condensed matter, materials, surfaces, interfaces, & biophysical chemistry*, 109(47):22181–22185, 2005.

[32] S. Orimo, Y. Nakamori, T. Kato, C. Brown, and CM Jensen. Intrinsic and mechanically modified thermal stabilities of α-, β-and γ-aluminum trihydrides AlH 3. *Applied Physics A: Materials Science & Processing*, 83(1):5–8, 2006.

[33] G. Sandrock, J. Reilly, J. Graetz, W.M. Zhou, J. Johnson, and J. Wegrzyn. Accelerated thermal decomposition of AlH_3 for hydrogen-fueled vehicles. *Applied Physics A: Materials Science & Processing*, 80(4):687–690, 2005.

[34] C. Wong and P.J. Miller. Vibrational Spectroscopic Studies of Alane. *Journal of Energetic Materials*, 23(3):169–181, 2005.